2008-12-22

Superconducting Iridium Thin Films as Transition Edge Sensors

Daniela Florentina Bogorin
University of Miami, daniela_bogorin@yahoo.com

UNIVERSITY OF MIAMI

SUPERCONDUCTING IRIDIUM THIN FILMS AS TRANSITION EDGE SENSORS

By

Daniela F. Bogorin

A DISSERTATION

Submitted to the Faculty
of the University of Miami
in partial fulfillment of the requirements for
the degree of Doctor of Philosophy

Coral Gables, Florida

December 2008

UNIVERSITY OF MIAMI

A dissertation submitted in partial fulfillment of
the requirements for the degree of
Doctor of Philosophy

SUPERCONDUCTING IRIDIUM THIN FILMS AS TRANSITION EDGE SENSORS

Daniela F. Bogorin

Approved:

_____ Massimiliano Galeazzi, Ph.D. Professor of Physics	_____ Terri A. Scandura, Ph.D. Dean of the Graduate School
_____ Joshua L. Cohn, Ph.D. Professor of Physics	_____ Fulin Zuo, Ph.D. Professor of Physics
_____ Maria Ribeiro Gomes, Ph.D. Professor of Physics University of Lisbon, Portugal Center for Nuclear Physics	

BOGORIN, DANIELA FLORENTINA (Ph.D., Physics)

Superconducting Iridium Thin Films as Transition Edge Sensors (December 2008)

Abstract of a dissertation at the University of Miami.

Dissertation supervised by Professor Massimiliano Galeazzi

No. of pages in text. (89)

Transition edge sensors are the detectors of choice for a wide range of applications; from dark matter search, neutrino search, to cosmic radiation detection from near infrared to millimeter wavelengths. We are developing transition edge sensors using superconducting iridium thin films and we are proposing their use for future dark matter and neutrino search experiments. Our Ir films are deposited using an radio frequency (RF) magnetron sputtering and photolithographic techniques and measured using an adiabatic refrigerator capable of reaching temperatures of a few tens of mK. This thesis presents a detailed description of superconducting iridium thin films from the fabrication process to the characterization of the film properties at room temperature and low temperature. Alternative options for the bias circuit used to read out the TES signals will be discussed, we are proposing the use of RLC resonant circuits and transformers instead of SQUIDS.

In the memory of my father

Acknowledgements

First, I must thank my friends and family, the people who have stuck by my side in hard times. All of you know who you are.

Second, I am deeply thankful to my advisor, Dr. Galeazzi, who opened the door to the world of low temperature physics for me, and made me a better "junior researcher." I am also grateful to Dr. Gomes, who taught me a lot in our conversations; to all my comity members; to Dr. Cohn for allowing me to use a good part of his equipment and always had good advice for me, and to Dr. Zuo, for his enquiring questions.

My deep respect and thanks are extended to other members of our department, especially Dr. Caroline VanVliet for believing in me; and all the others.

Of course graduate student life is empty without your lab mates and friends. Thank you all, it's been a fun ride. I hope we keep in touch.

TABLE OF CONTENTS

LIST OF FIGURES

Chapter 1

Introduction

In the last twenty years, the rapid development of cryogenic detectors operating at milikelvin temperatures had allowed impressive improvements in the sensitivity and precision of various types of applications. Microcalorimeters operating with Transition Edge Sensors (TES) are becoming the detectors of choice for radiation detection from radio, microwave, infrared, to X-ray, gamma rays, and particles. They are the engine behind large telescopes operated on the high mountains, balloon borne experiments and satellites looking in the deep sky. Large dark matter search experiments (e.g. CDMS) are also operated with the use of transition edge sensor detector arrays. Superconducting TES are capable of imaging spectroscopy with high energy resolution and quantum efficiency, combined with the ability to be used on extended sources without spectral degradation.

The present work is focused on developing transition edge sensors using superconducting iridium thin films for future dark matter and neutrino search experiments. The second chapter will present the motivation for this work. The third chapter will consist of background information and the operation theory of cryogenic microcalorimeters with transition edge sensors. The fourth chapter will present a full characterization of iridium thin films at room and low temperatures, together with a subchapter dedicated to microcalorimeter detector design. The

fifth chapter will present a proof of concept for two alternative readout options for transition edge sensors using transformers and RLC circuits. The thesis will close with a chapter consisting of conclusions, open questions and future proposed work.

Chapter 2

Background information

2.1. Motivation

We are in the golden age of cryogenic microcalorimeter detectors with applications which include high resolution photon detection from gamma rays, x-ray spectroscopy, UV-optical, IR-spectroscopy, IR bolometry, and CMB bolometers, the search for dark matter in form of WIMPs (weakly interacting massive particles), neutrino search, material physics, Lamb shift experiments and nuclear waste measurements [1]. However the concept of calorimeters is as old as 120 years.

The principle of detection of radiation using thermal energy has been used since the end of the nineteenth century and it is based on the first principle of thermodynamics. As a few notable examples from the history of physics we can mention Langley [2] (1880) who developed a resistive bolometer in order to investigate the infrared radiation emitted by the sun. In 1903, Curie and Laborde [3] successfully detected radioactive particles using the heat they generated. The idea of cryogenic calorimetric detection was first proposed and used by Simon [4] who stated that the sensitivity to thermal radiation can be improved if the detectors are operated at low temperatures. The first superconducting cryogenic detector was reported in 1949 and it was used for detecting individual alpha

particles [5]. The modern chapter of cryogenic microcalorimeters was introduced in 1984 when novel low temperature particle detectors were proposed for applications in nuclear physics, astrophysics and astronomy [6].

Cryogenic particle detectors can be separated in two main categories: non-equilibrium and near-equilibrium detectors [7]. Thermal detectors operating in a non-equilibrium mode are collecting quasi-ballistic phonons or are using sensors sensitive to energies in the k_BT range, were k_B is the Boltzmann constant and T is the temperature. In general, non-equilibrium detectors are faster than the equilibrium ones, but are very sensitive to the channel absorption position dependence and detection efficiency. This makes them used for application that do not require a very high energy resolution but require fast detection or position sensitivity. Near-equilibrium detectors offer a very high energy resolution, all detection channels are in thermal equilibrium, in theory there is no limit to the resolution efficiency that can be achieved [8].

I will be focusing on near-equilibrium detectors and in particular on cryogenic microcalorimeter that use a superconducting transition edge sensor for detecting the change in temperature.

Our interest in developing cryogenic detectors is driven by two challenging problems in the contemporary physics: measuring the mass or reducing the upper limit on mass of electron neutrino and studying the nature of the dark matter that accounts for about 30% of our Universe.

2.2. Neutrino physics

Neutrinos are fundamental particles capable of traveling with velocities close to the speed of light and almost undisturbed through baryonic matter. Neutrinos are leptons with zero electrical charge, so they are affected only by the weak force. This allows neutrinos to travel long distances through matter without being affected by it. It is now observed (e.g. neutrinos oscillations in SNO and Super-Kamiokande experiments) and demonstrated that neutrinos have a mass; however the value of the mass has not been determined yet.

Recent and present experiments are trying to measure or at least set a closer limit for the mass of the neutrino. For example a limit of 50eV on the υ_{υ}, was found using experiments on the decay of pions creating neutrinos. The strongest upper limit on the neutrino mass comes from cosmological data such as cosmic microwave background radiation, galaxy surveys and Lyman-alpha forest indicating that the sum of the neutrino masses must be less than 0.3eV [9] At this moment a number of experiments are on the way with the common goal of directly determining the absolute neutrino mass in the laboratory.

The experimental technique, which is sensitive to the absolute mass of the electron antineutrino, in a model-independent way, is the β-decay endpoint measurement. In a nucleus which undergoes β-decay a neutrino and an electron are emitted, see equation 2.1.

$$(A, Z-1) \rightarrow (A, Z) + e^{-} + \overline{\nu_e} \qquad 2.1.$$

where Z is the atomic number and A the mass number

While the neutrino escapes undetected, we can measure the energy spectrum of the emitted electron. The electron energy spectrum, $N_\beta\ (Z,E_\beta,m_{\upsilon e})$, is a rapidly falling function of energy reaching a maximum value determined by energy difference of the nuclear initial and final states and the mass of the electron anti-neutrino according to equation 2.2.:

$$N_\beta(Z,E_\beta,m_{\upsilon e}) = p_\beta E_\beta (E_0 - E_\beta)\sqrt{(E_0 - E_\beta)^2 - m_{\upsilon e}^2 c^4}F(Z,E_\beta)S(E_\beta) \times$$

$$\times \left[1 + \delta_R(Z,E_\beta)\right] \qquad 2.2.$$

Where: p_β and E_β are the momentum and energy of the electron, E_0 is the energy available in the final state:

$$E_0 = M(A, Z-1)c^2 - M(A, Z)c^2 \qquad 2.3.$$

$F(Z,E_\beta)$ is a term which accounts for the effect of the nuclear wave function on the emitted electron called form factor; $S(E_\beta)$ is the form factor of the beta spectrum and contains the contribution of the electroweak interaction nuclear matrix element; $\delta_R(Z,E_\beta)$ is the radiative electromagnetic correction, usually neglected.

Figure 2.1. shows the region near the endpoint of the β-decay spectrum, highlighting the difference in shape for the case of a neutrino with zero/non-zero mass. The fraction of events near the endpoint is quite small and is given by:

$$f_{\Delta E}(m_\upsilon = 0) \approx \left(\frac{\Delta E}{E_0}\right)^3 \leq 10^{-5} \qquad 2.4.$$

The MARE experiment (Microcalorimeter Arrays for a Rhenium Experiment) is proposing the use of a single beta decay of ^{187}Re, a very sensitive process due to the very low energy available to the particles in the final state

Q~2.5eV, [10], using a full kinematical approach. The neutrino mass will be determined from the shape of the beta spectrum in the region close to the end point Q.

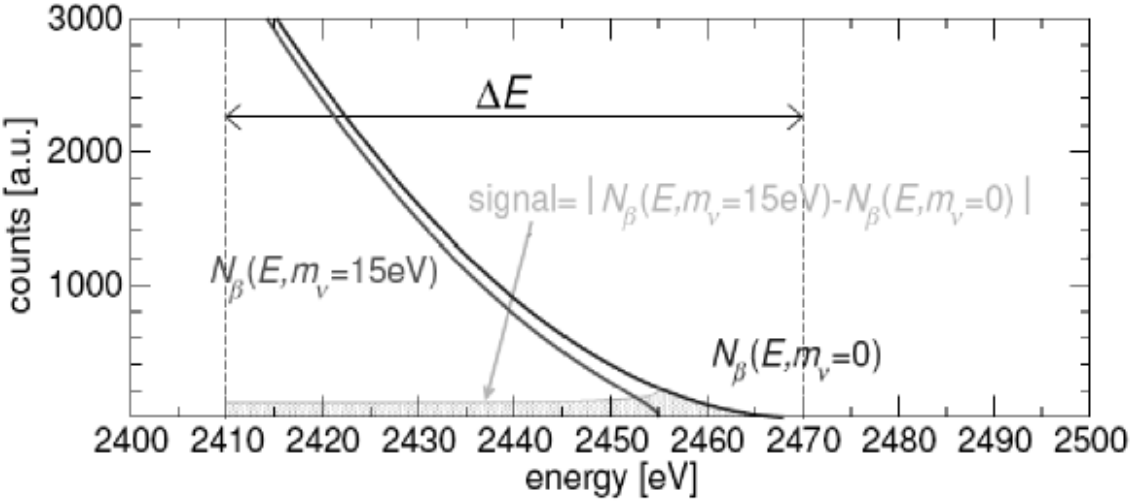

Figure 2.1. Kurie plot of a β-decay spectrum, near the endpoint region, comparing the two cases for $m_{\upsilon}=0$ and $m_{\upsilon}\neq 0$, courtesy of the MARE experiment collaboration

The current upper limit on the mass of υ_{υ}, using β decay is 2.2eV provided by the MAINZ and TROITZK experiments [11], from studies of ${}^{3}_{1}H$ beta decay (Q=18.6keV) using an electrostatic spectrometer. A larger expansion on the above mentioned experiments, named KATRIN is current development, with a projected sensitivity of 0.2eV. However there are a high number of systematic uncertainties related with these experiments and an alternative technique is highly desired [12].

The alternative to the electrostatic spectrometer approach is the use of a calorimetric method. The calorimetric approach has a number of advantages: it also measures the energy stored in excited states, there is no self-absorption

and no backscattering form the detector and no reflection on the source substrate. The main disadvantage of a calorimetric approach comes from the fact that the entire beta spectrum is recorded. Consequently one must keep a low count rate in order to keep a spectral shape without distortions.

In a calorimetric detection the ^{187}Re source is embedded in the detector and only the neutrino energy will escape the direct detection. The energy of the neutrino is measured in the form of the missing energy of the beta decay. The ^{187}Re beta decay

$$^{187}Re(5/2^{+}) \rightarrow {}^{187}Os(1/2^{-}) + e^{-} + \overline{\nu_e} \qquad 2.5.$$

has a transition energy of Q=2470±1(stat)±4(syst)eV (the lowest known in nature) and the half lifetime of, 4.12±0.02(stat)±0.11(syst)×10^{10}years, [13]. The large isotopic abundance (62.8%) of ^{187}Re in natural rhenium allows getting a useful source without any isotopic separation process. The beta decay rate in natural rhenium is of the order of 1 Bq/mg which makes it ideal for bolometric detection. When a nucleus decays, the total energy available to the e^{-} - $\overline{\nu_e}$ system (endpoint energy) is equal to the total energy available from the nuclear decay minus the energy of the internal state of the atom. In a calorimetric experiment the energy detected is the electron energy plus the energy of the excited atomic state and there is only one end point energy, equal to the total energy available in the nuclear decay. However, due to the fact that in a calorimetric experiment all the decays are detected (with energies close or far away from the endpoint) there is a need of huge amount of data to be acquired. ^{187}Re is a good candidate

since it has the lowest known energy endpoint, which means it is the isotope with the highest ratio between events near endpoint and total events.

The MARE experiment is proposed to be developed in two stages: MARE 1 has the goal of constraining the neutrino mass up to 2eV sensitivity, and MARE 2 to increase the sensitivity to 0.2eV.

The MARE experiment consists of multiple cryogenic microcalorimeters (about 300 pixels for the first stage) with ^{187}Re absorbers and iridium superconducting transition edge sensors, [13]. A detailed description of a cryogenic microcalorimeter principle of operation will be given in the next chapter.

2.3. Detection of dark matter

From astrophysical and cosmological measurements we know that about 95% of the composition of the Universe is unknown. There is about 5% baryonic matter, 20% non-baryonic cold dark matter (CDM) and about 70% dark energy [14]. The existence of dark matter is crucial for the Big Bang model in cosmology; this makes the search for dark matter one of the most exciting problems in cosmology.

When we think about dark matter candidates we are considering matter that does not interact with electromagnetic forces (does not have electrical charge) but can interact gravitationally with visible baryonic matter, its presence

can be deducted from observations of the motion of astronomical objects - rotations and collisions of galaxies (e.g. the Bullet cluster).

Due to the abundance of dark matter observed (deduced) cosmologically, the total annihilation cross-section could be determined assuming that the particles of dark matter are in thermal equilibrium with the rest of the Universe until the annihilation rate fell below the cosmological expansion rate. The resulting cross-section is consistent with particles in the mass range of GeV/c^2 – TeV/c^2. The interaction of these particles with ordinary matter is through the weak force, thus the name of WIMPs [16], [17].

There are a series of experiments that have as a goal the direct detection of WIMPs, to mention just a few: XENON, CRESST, CDMS, CDMSII, etc. Heavy dark matter particles can be detected directly by observing nuclear recoils in terrestrial detectors or indirectly by looking at the annihilation products, such as high-energy neutrinos, charged leptons, gammas. The sources of these annihilation products can be found in the sun, galactic halos and the galactic center. The WIMPs are expected to interact with the nuclei of the detector producing a recoil which is further detected.

Gaitskell summarizes about forty dark matter search experiments from 1985 to present, each using various methods of detection using: germanium ionization detectors, solid scintillation detectors NaI/CsI, liquid noble elements (Xe), gaseous detectors, axion detectors and cryogenic microcalorimeters [14].

In the case of the cryogenic detectors the detection of absorption of a dark matter particle is based on the sensing of nonequilibrum phonons. The absorber

is usually a semiconductor or a superconductor kept at very low temperatures so there is a very low number of free electrons. When a dark matter particle hits the nucleus of an atom from the crystal lattice, an avalanche of effects can be observed: the nucleus will recoil due to the scattering of the dark matter particle and will lose energy through collision with neighboring atoms of the crystal lattice, this produces phonons (due to the atom vibrating around the mean position). Due to the fact that the total recoil energy is large compared to the average phonon energy, the phonons will be distributed over the whole spectrum. These primeval phonons will propagate away from the recoil region and will decay producing secondary phonons with longer lifetime. The secondary phonons propagate ballistically to the surface of the absorber. Since the absorber is in contact with an array of sensors, every small change in the thermal energy due to phonon propagation and decay in the absorber is detected. The sensor's output is recorded over time. Depending on the frequency of the phonons detected the sensors must be of various types. A complete description of the phonon propagation in absorbers for dark matter particles can be found in [18].

The CDMS II experiment is using silicon and germanium crystals (1cm thick and 7cm in diameter) of high purity and quality of the crystal structure as absorbers and tungsten transition edge sensors arrays as sensors deposited on 10 cm diameter wafers [19]. The values of the transition temperature of the tungsten thin films can vary up to 100mK over a 10 cm diameter. This can present a major inconvenience since every detector will operate at a different temperature. By implanting Fe in different concentration on each detector of the

wafer the difference in the transition temperature can be reduced up to 20mK. The detectors are then individually calibrated. This is not a huge problem if we are working with a low number of wafers on a detector with a total mass up to 25kg mass (Super CDMS). For future experiments that are proposing the use of large arrays of microcalorimeters with transition edge sensors on detectors with a total mass reaching 1 ton or more having to individually calibrate and tune every sensor will present a huge obstacle.

We are considering the use of Iridium based sensors which will provide a better uniformity of the transition temperature over the whole diameter of the wafer with $\delta T \leq 4$ mK. Our results in testing the iridium thin films for transition edge sensors, (TESs) will be presented in chapters 4 and 5.

Chapter 3

Microcalorimeters with Transition Edge Sensors

3.1. Operation principle

Microcalorimeters are versatile and flexible devices. The linear theory of microcalorimeters is relatively well known at this moment and a series of reviews has been published [20-23]. However the linear theory has its own limitations and the manufacturing and development of microcalorimeters with transition edge sensors is not straightforward, for example the behavior of a superconductor at the superconducting phase transition is not well understood. In the following pages, I will summarize the operating principle for a cryogenic microcalorimeter detector.

A microcalorimeter has three main components: an absorber for the incoming radiation which will convert the incident energy (radiation) to phonons (thermal energy); a sensor in contact with the absorber that will detect the temperature variations of the absorber and a weak thermal link between the detector and a heat sink. The sensor can be a superconductor working at the transition temperature, in which case it is referred to as a transition edge sensor, TES. A schematic diagram of a microcalorimeter can be seen in Figure 3.1.

When incident radiation hits the absorber the energy is thermalized, that is, it is distributed between the electrons and thermal phonons. The temperature

of the absorber will increase abruptly and consequently the temperature of the sensor increases too. The temperature then decreases due to the weak thermal link to the heat sink and the effect of electro-thermal feedback, described in the following pages. The increase in temperature will be detected by the sensor and converted to a change in resistance.

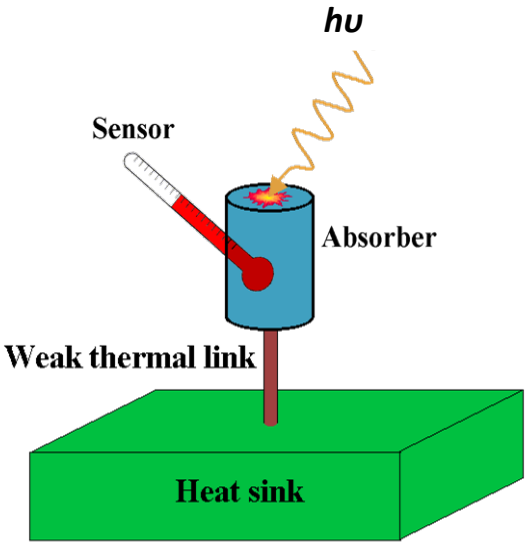

Figure 3.1. Schematic view of a cryogenic microcalorimeter

In the case of dark matter particle detection, the absorber will detect the phonon vibrations due to the recoil of a nucleus from the crystal structure hit by the incident particle before the absorbers is thermalized.

Knowing the operating principle it is possible to engineer our detectors depending on the energy interval of interest and the mechanism by which the thermal energy is absorbed. In order to have a fast detector with a high energy resolution, high quantum efficiency, which will thermalize fast and will go back to

the initial working point quick enough to be ready to detect the next incident radiation, we need to take in consideration the physical properties of its main components.

The absorber will have to be opaque to the incident radiation, and the main characteristics to consider will be the total collecting area, the efficiency and speed of the absorber in thermalizing the incident energy. For a good stopping power for high energy photons, usually a high Z material is chosen. For dark matter detection the absorbers can be a semiconductor crystal, an insulator, or a superconductor well below the transition temperature so the number of free electrons will be exponentially small. A very important parameter will be the purity of the crystal structure. The dark matter detectors are based on sensing (detecting) nonequilibrum phonons (lattice vibrations). An incident dark matter particle will scatter off a nucleus in the incident crystal; this will produce phonons which will be detected by the sensors positioned at the surface of the absorber. A good detector will have a low energy threshold being capable to detect small amounts of deposited energy. For example for the CDMS experiment a Ge or Si crystal of very high purity and lattice uniformity is used as absorber.

The sensor must be able to detect small temperature changes; this is described by the sensitivity parameter alpha, defined as:

$$\alpha = \frac{dlogR}{dlogT} = \frac{\mathrm{T}}{\mathrm{R}}\frac{\mathrm{dR}}{\mathrm{dT}} \qquad 3.1.$$

where T is the temperature and R the resistance of the sensor. The sensitivity is dimensionless and must be high in order to produce a large electrical response to a small temperature change. The sensor is usually a resistor with a strong

dependence of its resistance with temperature at the working point. Superconducting materials have a very strong resistance dependence on temperature between normal and superconducting state and are the optimal choice for sensors [24].

The energy resolution of microcalorimeters is limited by the noise in the detector. The noise sources are the Johnson noise of the sensor, thermal noise, phonon shot noise due to random flow of energy carriers through the weak thermal link, photon noise, electrical noise due to the read out circuit, and, in some cases a sensor excess noise of unknown nature.

In the first approximation we can assume the noise is dominated by the Johnson and thermal components [22]. The parameter used to quantify the noise in a detector is the Noise Equivalent Power (NEP), that is, the amount of power absorbed by the detector that would generate an output signal equivalent to the signal generated by the noise. Considering only the phonon and Johnson noise, the NEP is given by:

$$NEP^2 = NEP^2_{Johnson} + NEP^2_{phonon} \qquad 3.2.$$

where

$$NEP^2_{phonon} = 4k_B G T^2 \int_{T_C}^{T} \left(\frac{t' k(t')}{T k(T)}\right)^2 dt' \Big/ \int_{T_C}^{T} \frac{k(t')}{k(T)} dt' =$$

$$= \frac{4k_B T_C^2 G t^2 \left(1 - t^{-(3+2\beta)}\right)(\beta+1)}{(3+2\beta)(1-t^{-(\beta+1)})} \qquad 3.3.$$

$$NEP^2_{Johnson} = 4k_B T_c^2 G t^2 \, (\beta + 1)/\alpha^2 (1 - t^{-(\beta+1)}) \qquad 3.4.$$

where $t = T/T_C$; T_C is the heat sink temperature, T is the temperature of the sample, G is the differential thermal conductance of the heat link defined as the

derivative of the conducted power with respect to the sample temperature T, k is the function describing the temperature dependence on the thermal conductivity of the heat link material $k \approx T^{\beta}$, and α is the sensitivity of the sensor as defined in equation 3.1.

From the NEP it is possible to compute the energy resolution of the microcalorimeter using the expression [29]:

$$\Delta E_{RMS} = \frac{1}{\sqrt{\int_0^{\infty} \frac{2d\omega}{\pi NEP^2(\omega)}}} \qquad 3.5.$$

Using the equations for the Johnson noise and phonon noise we obtain in the first approximation the energy resolution as:

$$\Delta E \approx \sqrt{\frac{4k_B T^2 C}{\alpha}} \qquad 3.6.$$

where C is the heat capacity of the absorber, k_B is the Boltzmann constant, T is the temperature of the detector, and α is the sensitivity, [23].

3.2. Microcalorimeter operation

The weak thermal link to the heat bath of the microcalorimeter must be relatively high so the detector will be back at the operation point fast enough to detect the next absorption event but small enough to allow the temperature to increase. In a first order approximation, the rise in the microcalorimeter temperature is proportional to the incident energy and inversely proportional to the heat capacity of the absorber.

$$\Delta T = \frac{E}{C} \qquad 3.7.$$

Ideally we desire a detector with the best possible energy resolution and high count rate. The intrinsic time constant τ of the detector, depends on the thermal conductance of the weak thermal link to the heat bath G and the heat capacity of the absorber C.

$$\tau = \frac{C}{G} \qquad 3.8.$$

Notice that the actual time constant of the detector may be much faster due to the effect of electrothermal feedback. The TES is usually voltage biased and the temperature in the microcalorimeter is higher than the temperature of the heat sink due to the Joule power dissipated in the TES resistance. The electrothermal feedback is due to the fact that the Joule power decreases when the temperature increases due to radiation events. The electrothermal feedback is negative in this case and the TES can be “self-biased” improving stability [23].

To quantify the effect of the ETF on the speed we can use a “virtual conductance” associated with the ETF (electrothermal feedback), so the effective time constant will become:

$$\tau_{EFF} = \frac{C}{G+G_{ETF}} \qquad 3.9.$$

with

$$G_{ETF} = \frac{P\alpha}{T}\frac{R-R_L}{R+R_L} \qquad 3.10.$$

where P is the power dissipated in the detector at the equilibrium, α is the sensitivity of the TES, R and R_L are characteristics of the bias circuit. In the case of TESs the α is positive and large so the intrinsic time constant may be of the order of 0.1-1ms. Equation 3.9. and 3.10. will be derived in the next section.

The bias circuit for a typical sensor is illustrated in Figure 3.2. Usually the TES is biased at a constant voltage and coupled with the input of a superconducting quantum interference device, SQUID. A SQUID is a magnetometer used as a current transducer.

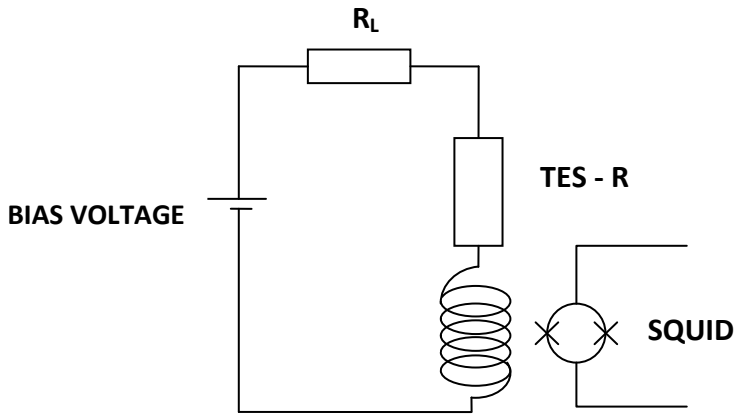

Figure 3.2. Schematic bias diagram for TES readout

The resistances of the superconducting thin films used are usually below 1 Ohm, the TES is biased and kept at the low end of the transition about 20-30% away from the zero resistance.

When energy is absorbed in the TES the temperature increases and so does the resistance of the superconducting thin film, generating a very sharp drop in current as showed in Figure 3.3. The temperature will then return to the original value due to the weak thermal link to the heat sink and the electro thermal feedback.

Microcalorimeters are usually operated around 100mK. The number of pure superconducting materials that show the transition temperature

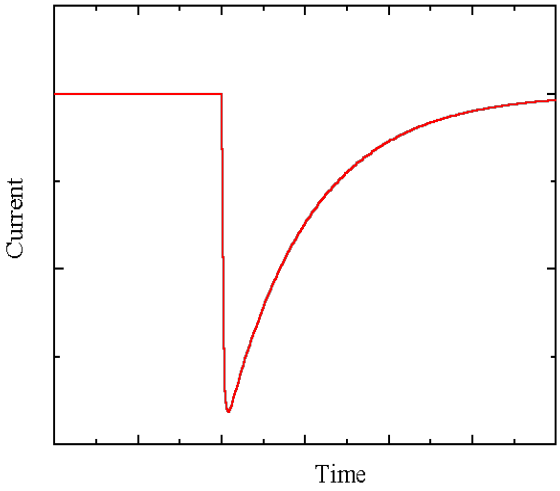

Figure 3.3. The variation in time of the current through the bias circuit due to heat.

in this range is limited and many groups working in the transition edge sensors development are using bilayers of superconductor thin films and normal thin films. It is well known that adding a thin layer on normal metal the transition temperature of the superconductor will be decreased due to the proximity effect [25], [26]. So, we can obtain a desired transition temperature by choosing the correct thickness of the superconductor and normal thin films [27]. The most used combination of bilayers thin films are Mo-Cu, Mo-Au, Ti-Au and Ir-Au. In the case of W thin films a reduction in transition temperature is provided using implantation of ferromagnetic materials (e.g. Fe). The shape of the transition, which will determine the sensitivity α and it is somewhat dependent on the geometry of the TES. We are proposing the use of a single layer of Iridium superconductor for our TES and through the next chapter we will full characterize the properties of iridium thin films.

3.3. Linear theory of microcalorimeters

The nonequilibrum theory of bolometers with ideal resistive thermometers has been developed by Mather, [22],[28] and an extension for microcalorimeters performance was first introduced by Moseley et al (1984), [29]. A more recent and complete model for a microcalorimeter was proposed by Galeazzi (2003, 2004), [30], [31].

An ideal microcalorimeter can be modeled in first approximation by an absorber with a heat capacity C, in contact with a heat sink through a thermal conductance G, and a thermometer that is at the same temperature as the absorber T. At the absorption of a certain amount of power W, the microcalorimeter temperature will rise by ΔT. In the first order approximation the change in temperature satisfies:

$$C\frac{d\Delta T}{dT} + G\Delta T = W + \Delta P \qquad 3.11.$$

where ΔP is the change in the Joule power dissipated in the thermometer due to the increase in temperature called electrothermal feedback, as described in the previous paragraph. We assumed that the change in temperature is very small $\Delta T \ll T$ and we work in the first order approximation only.

The thermal conductance is defined as

$$G \equiv \frac{dP}{dT} = G_0 T^{\beta} \qquad 3.12.$$

where P is the power dissipated in the detector and G_0 is a proportionality factor numerically equal with the thermal conductance at 1K but with the units of a thermal conductance divided by the temperature at a power β.

At equilibrium using just the Joule power used to read out the resistance of the TES, the equilibrium temperature is given by integrating equation 3.12. with the limits between the temperature of the heat sink T_S and the detector temperature.

$$T^{\beta+1} - T_S^{\beta+1} = \frac{\beta+1}{G_0} P(T) \qquad 3.13$$

where the power depends on the value of the sensor resistance and it therefore depends on the temperature T.

The electrothermal feedback plays a crucial role in the response of the detector, and for a typical detector readout as seen presented in the previous paragraph, can be calculated as follow:

The Joule power can be written as:

$$P = I^2R = V^2R \text{ were } I = V_0/(R + R_L) \qquad 3.14.$$

where V_0 is the bias voltage. Differentiating the Joule power expression $P = \left(\frac{V}{R+R_L}\right)^2 R$ using the bias circuit we will obtain an expression for the ΔP as: $\Delta P = \frac{\partial P}{\partial R}\Delta R$ Using the definition for α (equation 3.1.) we obtain: $\Delta P = \frac{\partial P}{\partial R}\alpha\frac{R}{T}\Delta T$ which becomes:

$$\Delta P = -\frac{P}{T}\frac{R-R_L}{R+R_L}\alpha\Delta T \qquad 3.15.$$

We can then write Equation 3.15. as $\Delta P = -G_{ETF}\Delta T$ with G_{ETF} defined in Equation 3.10.

Equation 3.11. then becomes:

$$C\frac{d\Delta T}{dT} + (G + G_{ETF})T = W \qquad 3.16.$$

We can introduce an effective thermal conductance for the heat sink that adds a correction for the electrothermal feedback to the thermal conductance G.

$$G_{eff} = G + G_{\ ETF} \qquad 3.17.$$

To solve Equation 3.11., the easiest approach is to use Fourier transforms to convert the terms of the eq 3.14. to frequency domain were it will become linear. The derivation has been reported by Galeazzi et. al. (2003), [30].

The advantage comes from the fact that the expression $d\Delta T(t)/dt$ becomes $j\omega\Delta T(\omega)$ with $j = \sqrt{-1}$.

The equation 3.16. can be written in the frequency domain as:

$$j\omega C\Delta T(\omega) + G_{eff}\Delta T(\omega) = W(\omega) \qquad 3.18.$$

This equation can be solved for ΔT:

$$\Delta T = \frac{1}{G_{eff}}\frac{1}{1+j\omega\tau_{eff}}W(\omega) \qquad 3.19.$$

where $\tau_{eff} = C/G_{eff}$

The detector system will behave as a low-pass filter with a time constant

$$\tau_{eff} = \frac{C}{G_{eff}} = \frac{C}{G+G_{ETF}} \qquad 3.20.$$

If the electrothermal feedback is negative, the G_{ETF} is positive and the effective time constant of the detector is shortened.

The ideal model of a microcalorimeter predicts that the performance of the detector will increase dramatically as the temperature decreases, however for temperatures below 200mK it is very difficult to fabricate a detector that will operate only in the limits of the linear theory.

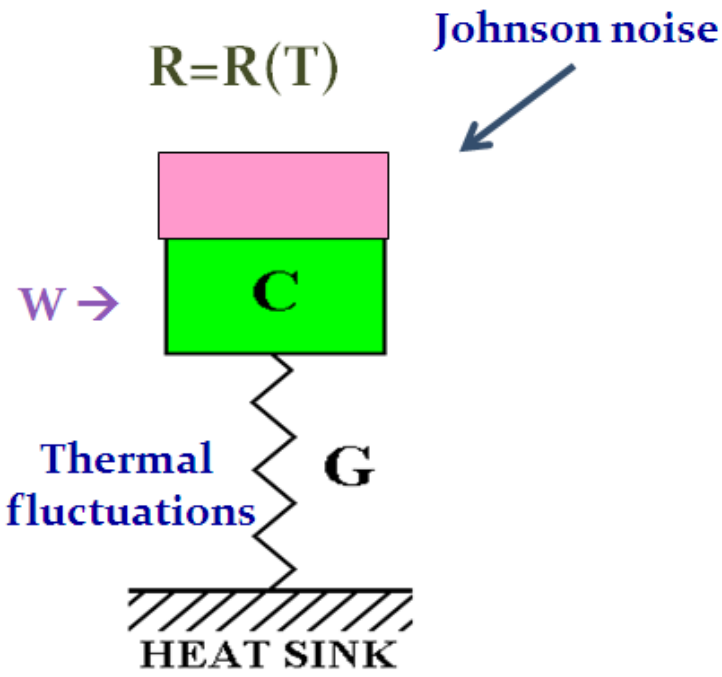

Figure 3.4. Thermal sketch of a microcalorimeter, the thermometer (shown in pink) has its resistance dependent of temperature and its performance is limited by the Johnson noise.

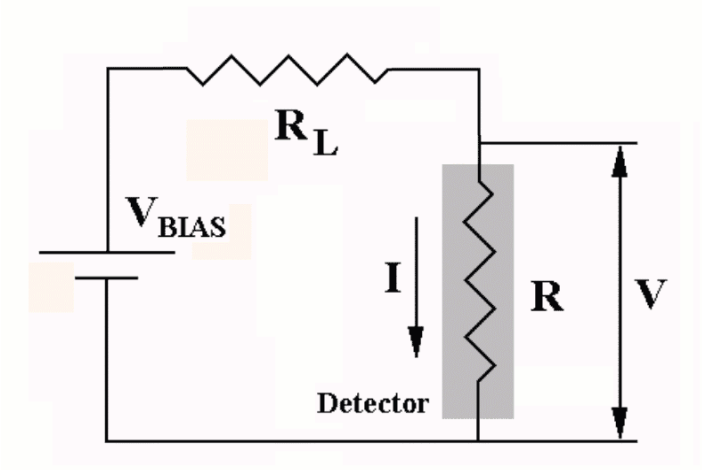

Figure 3.5. Detector readout circuit, usually a transition edge sensor is voltage biased, with $R_L >> R$.

Thermodynamic fluctuations between the individual parts of the microcalorimeter act as additional noise sources. As a result, the temperature of

the TES depends not only on the bias but also on the temperature and equilibration time between the individual parts connected to it. A complete treatment of non-ideal effects can be found in Galeazzi et al (2003).

Despite the fact that the manufacturing process and optimization of microcalorimeter detectors is not straightforward, impressive results have been obtained. For example, in the soft X-ray band, the microcalorimeters developed at NASA have a 2eV FWHM at 6keV.

Chapter 4

Iridium thin films for Transition Edge Sensors

4.1. Background

Several recipes have been suggested and used for the fabrication of transition edge sensors. In addition to good performance, the choice of the material depends on long term stability both physical and chemical along with a good reproducibility and uniformity in fabrication.

For this purpose we are investigating the properties of iridium (Ir) thin films. Iridium has a bulk transition temperature of 113 mK [32], making it suitable for the fabrication of TES detectors without the need for more complex bilayers. Due to a high melting point, around 2719 K and to the fact that a very small amount of ferromagnetic impurities can change the transition temperature drastically (a few parts per million), we chose to deposit the Ir films using a dedicated RF magnetron sputtering system.

As part of this work first we developed a recipe for the iridium thin depositions. Then we verified the quality of our devices from both the reproducibility and uniformity standpoint and investigated the sensitivity to bias currents, critical currents and the variation of the transition temperature with the thickness of the thin films.

The superconductivity of Ir has been reported for the first time in 1962, [33] but its properties have not been fully employed until the recent development of cryogenic techniques and the need for low temperature detectors.

Thin film depositions of Ir have been previously reported using various techniques like pulsed laser deposition (PLD) [34], chemical vapor deposition [35], electron beam evaporation, D.C. or R.F. magnetron sputtering [36]. For our applications we need to be able to deposit thin films with a very high purity and thickness uniformity over large areas. The high purity will insure a very sharp transition between the superconducting and normal state and thus a very high sensitivity α. We found that the transition temperature is dependent on the thickness of the thin film; therefore a high uniformity will provide a uniform transition temperature over the four inch substrate wafer.

4.2. Manufacturing process

The iridium thin films studied for this project have been deposited using an AJA International, Radio Frequency (RF) magnetron sputtering model ATC ORION 4 HV with load lock [37]. The magnetron is equipped with two targets for aluminum and iridium but it can be upgraded to four targets. The deposition chamber is kept under high vacuum (1×10^{-7}torr) at all times in order to insure a clean environment. To load the samples in the deposition chamber we use a load lock chamber that reaches low pressures (~10^{-6} torr) in just a couple of minutes, so it is possible to manufacture more than a sample a day. The substrate on

which we deposit our films is rotating at uniform speed in order to insure a uniform layer and can be heated up to temperatures of 800°C. The substrates used for this project were polished four inch Si[100] wafers or Si wafer with a 2 microns silicon nitride - Si_3N_4 coating. The wafers are cleaned using 99.999% pure acetone in an ultrasound bath for 10 minutes, then rinsed with 99.999% pure ethanol to remove the acetone and finally thoroughly rinsed with pure deionizer water.

The thin film manufacturing facilities at the University of Miami, Physics Department, consists of a self build dust free clean room kept under positive pressure. The air entering the clean room from outside is filtered via a large HEPA filter running at all times, there is an anteroom and a curtain at the entrance of the clean room, the preparation tables also have two large HEPA filters running at all times.

In order to deposit patterned iridium thin films photolithographic techniques have been used. Our clean room is equipped with a 2 to 4 inch spinner from Headway Research Inc. model: PWM 32-PS-R790, and a two inch photolithographic system from Oriel Instruments equipped with an arc lamp with powers from 200-500W Hg for wafer processing.

The wafers are coated with S1813 Shipley negative photoresist, the thickness used ranging from 1500nm to 1050nm, obtained by spinning the wafer at velocities between 3000RPM and 6000RPM, and then dried for 60 seconds on a hot plate at 100°C. The desired pattern is imprinted on the photoresist with a 3

second exposure to an ultraviolet arc lamp (P=450W) then the unwanted photoresist is removed using a MF-319 developer (1 min).

The iridium deposition recipe has been developed as a part of the work for this thesis. In order to have a stress free, pure iridium thin film we deposit a few atomic layers of aluminum thin film to improve the adhesion between the Si(100) wafer and the Ir. The lattice constant for aluminum is in fact in between the ones of iridium and silicon; a=b=c=5.431Å for Si, a=b=c=4.05Å for Al and a=b=c=3.84Å for Ir. For thicker Ir films we always deposit and Al layer underneath the Ir to improve the adhesion. The Al layer is thin enough so it will not affect the transition temperature due to proximity effect in superconductor/normal material bilayers. Once the patterned silicon wafers are rinsed and dried they are loaded in the load lock chamber, and the pressure is lowered below 10^{-6}mtorr. At that time the load lock can be opened and the sample is inserted in the deposition chamber. The depositions are made in pure argon vapor usually at 5mtorr pressure. The substrate loaded with the Si wafer is heated at 100°C for 30 minutes and rotated to keep uniform temperature; this insures that the wafers are dry and clean. The temperature is then decreased to 30C at which time the deposition can proceed.

The magnetron sputtering operation is a well established deposition method. The sputtering process creates first pure argon plasma with accelerated ions. The ions are hitting the source (cathode) and remove atoms/clusters of atoms by energy transfer, the atoms are deposited on a substrate (anode,

usually a Si wafer). A sputtering system requires an energy source (R.F., D.C. or M.W.) in order to create and maintain the ionized plasma.

Our choice for a R.F. magnetron sputtering deposition system was justified in part by the uniformity of the layers deposited over a 4 inch diameter due to the arrays of magnets behind the source as shown in the Figure 4.1.

The use of magnets behind the source is used to trap free electrons close to the target. These electrons follow helical trajectories around the magnetic field lines and improve greatly the rate of ionization of the neutral argon gas molecules and thus a higher deposition rate. The sputtered atoms are neutrally charged and are not affected by the magnetic field.

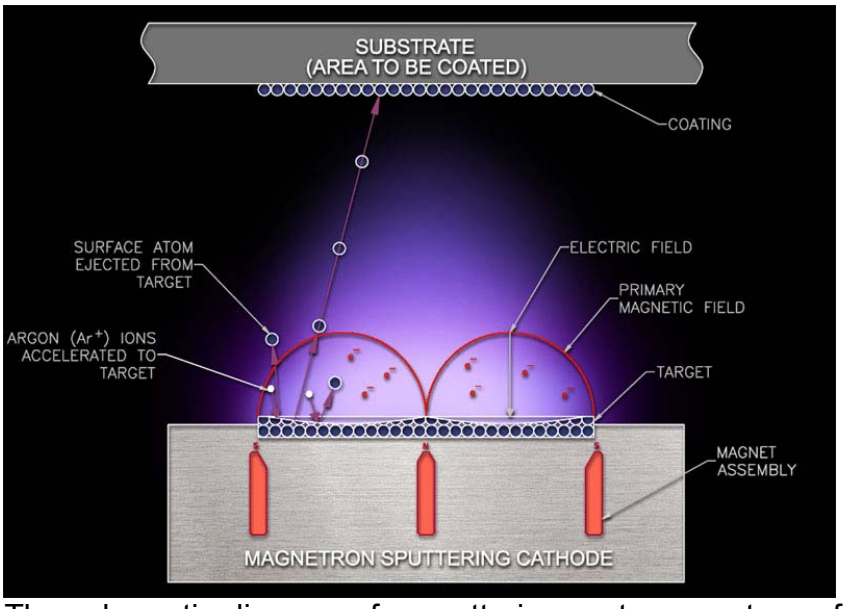

Figure 4.1. The schematic diagram of a sputtering system courtesy of Angstrom science [38]

In our setup, see Figure 4.2., the plasma is ignited at a pressure of 20 mtorr then the pressure is lowered to 5 mtorr. Before any deposition the sources are kept running with the shutter closed for 10 minutes. First a two minutes

aluminum deposition is made keeping the distance between the source and target at about 10cm. The iridium deposition is made keeping the distance between the source and target at about 7.5 cm. We use the same argon pressure for both the deposition of Ir and Al. The RF power for Al is always 30W, while for the Ir we vary the power between 30W and 90W. For our tests we deposited iridium films of thicknesses between 10Å to 5400Å.

Figure 4.2. Picture of our magnetron sputtering, notice the load lock

4.3. Room temperature characterization of the iridium films

We investigate first the properties of the Ir thin films at room temperature. We need to study the composition and purity of our iridium thin films.

4.3.1. General description

To determine the crystal structure of the thin films deposited we used a Philips X'pert X-Ray Diffractometer (XRD). **T**he x-ray source used in the XRD is a ceramic filament tube with a Cu-target. The filament is made of tungsten and it is normally operated at 40 kV and 15 mA. **C**u gives a K_α of 1.542 Å and K_β of 1.3922 Å, unwanted K_β radiation is eliminated by a Ni filter, which will decrease the K_β intensity by 98% and the K_α by 48%.

For our application we use the K_α incident X-rays with 1.54Å and a typically the filament at 45kV and 15mA to obtain a high resolution spectra. The reflected radiation is counted by a detector – a Xe-filled proportional counter equipped with a filter slit (parallel beam optics), the output will be measured in intensity (counts per second as a dependence of the θ). **T**he focal spot is 12 mm × 0.4 mm. The tube can have either a point focus or a line focus. For the determination of the crystal peaks we used a 2θ-ω scan using the in line focus.

4.3.2. Thickness measurement of the iridium thin films

We used the XRD for measuring the thickness of the thin films via a grazing incidence measurement X-ray reflectometry (XRR), this is a very important test for us since, as we will discuss later, the properties of the iridium thin films are dependent of the thickness. Unfortunately the method can be used only for films with thicknesses of 2-200nm with a precision of about 1-3Å. This

technique however, has the advantage is a nondestructive noncontact high precision method.

We used this thickness measurement to calibrate our deposition system. We measured the thickness of thinner films and using the thickness measured together with the deposition parameters we obtained a first approximation for the thickness of iridium films.

Figure 4.3. Philips X'pert Diffractometer

XRR method involves monitoring the intensity of the x-ray beam reflected by a sample at grazing angles. A monochromatic x-ray beam of wavelength λ irradiates a sample at a grazing angle ω (between 0-5 deg) and the reflected intensity at an angle 2θ is recorded. The angles satisfy the condition $2\theta=\omega$; the incident angle is always half of the angle of diffraction. The sample is rotated such that the rotation axis lies on the sample surface.

The reflection at the surface is due to the different electron densities in the different layers, for a incident angle below a critical value θ_C we would obtain total external reflection. Above θ_C the x-ray penetrates the thin film and we observe a interference picture between the reflected waves at the top and the bottom in the crystal lattice and we obtain interference fringes dependent on the angle of incidence.

In our thickness measurement tests we measured iridium thin films deposited for 5 minutes to one hour, see Figure 4.6. The results are consistent with each other and with the thickness measured using a profilometer, see the detailed description in the next paragraph.

The XRD diffraction measurements are based on the Bragg's law

$$n\lambda = 2d\ sin\theta \qquad 4.1.$$

Where n is the order, n=0,1, 2,….; λ is the wavelength, d is the thickness and θ is the incident angle of the X-ray radiation on the film.

Using equation 4.1. we can determine the thickness as:

$$d = \frac{\lambda}{2}\frac{1}{\theta_{m+1}-\theta_m} \qquad 4.2.$$

In general the difference on the angles θ_m and θ_{m+1} is determined from the interference fringe picture as shown in figure 4.4.

The precision of the method can be as small as 1Å. From Figure 4.4. we can also get information about the uniformity of the thin film. The difference between m and m+1 orders should be the same for a perfect film.

In the figure 4.4. the thickness of the two films (in blue and green) is calculated for consecutive interference peaks. Notice that the difference in the

intensity of the fringes between the two samples is probably due to alignments in the system

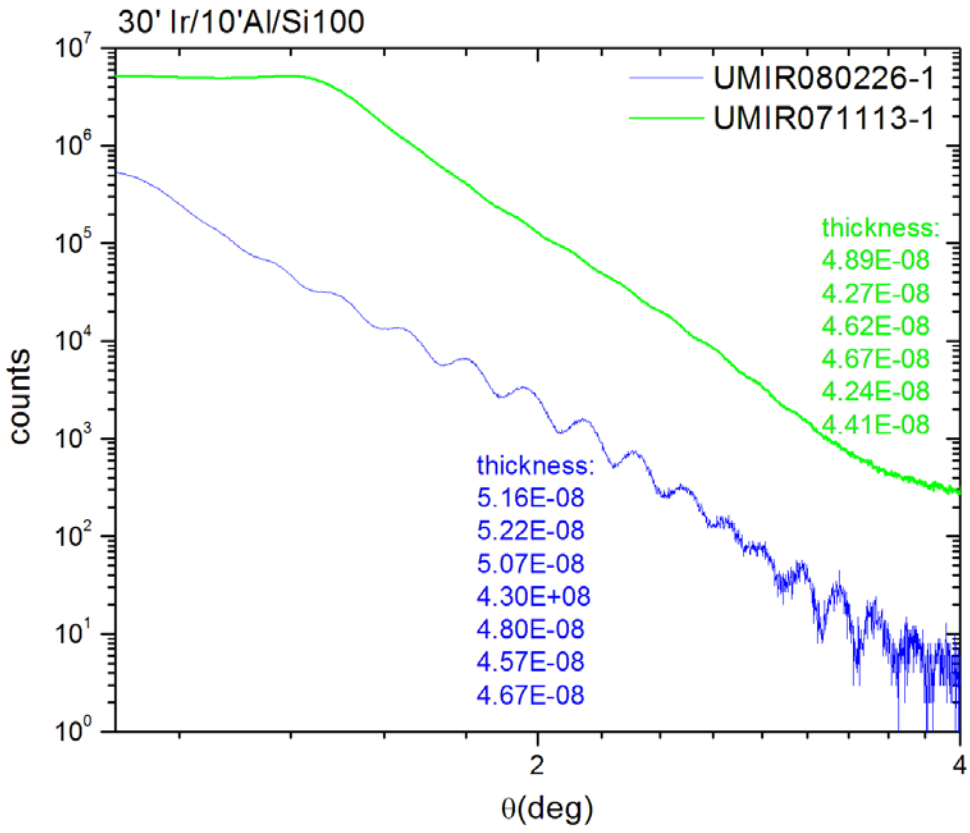

Figure 4.4. Comparison between the thicknesses of two films deposited with the same recipe at a distance of a couple of months apart, this test was done to investigate the variation in thickness due to the thinning of the iridium magnetron sputtering target. The thickness values are expressed in m.

To verify the accuracy of our thickness estimates for thicker films, we measured directly the thickness of a ten films using a profilometer, in collaboration with University of Lisbon/Center for Nuclear Physics.

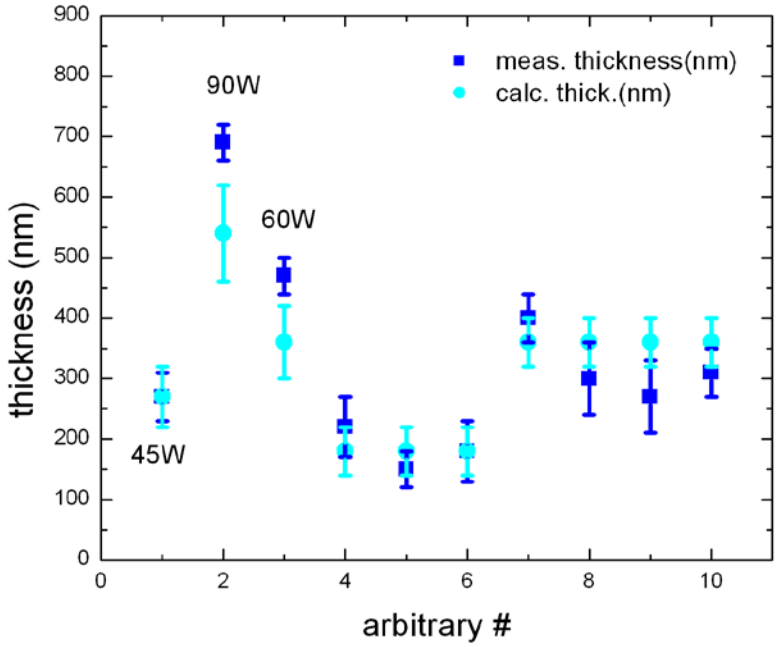

Figure 4.5. Comparison between the measured and calculated thicknesses of some of the samples presented in this paragraph,

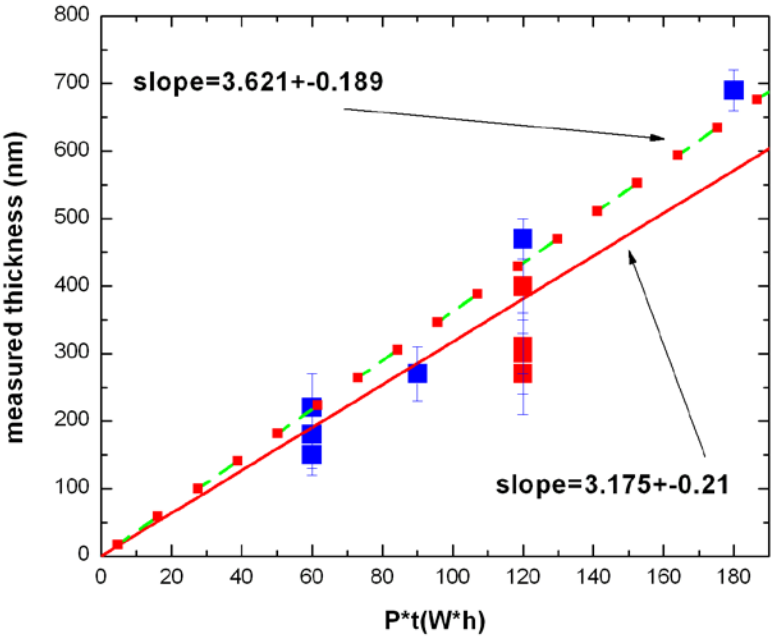

Figure 4.6. Linear fit for the measured thickness with respect of the deposition parameters: time and RF power

In Figure 4.5. we present a first comparison between calculated and measured thickness for the samples measured at the University of Lisbon/Center for Nuclear Physics. The x axis has arbitrary incremental numbers to separate the different films. The samples from 1-3 have been deposited at 45W, 90W and 60W R.F. power, all rest have been deposited at 30W power for two hours (samples 4-6) and four hours (samples 7-10). Calculated and measured thicknesses are in agreement within the error bars, supporting our method of estimating the thickness and confirming the good reproducibility of the R.F. sputter system.

For a more accurate analysis, we plotted in Fig. 4.6 the measured versus calculated thickness. For a more straightforward comparison, we used directly the product of the sputtering power times the deposition time for the calculated thickness. In the figure the points shown in light blue are for samples obtained during 4 hour depositions; all the others are from 2 hour depositions. As the plot shows, the two 2 hour samples follow a linear dependence of thickness versus power, confirming the assumption that the sample thickness scales linearly with power. However, the 4 hour samples, although they are still consistent with a linear scaling, seem to be systematically thinner. The two lines in the plot represent the linear fit to all the data points (continuous red line) and to only the two hour samples (dashed green line). Assuming that the lower thickness is real and not just due to statistical fluctuations, it may be due to overheating of the target that reduces the efficiency of the sputtering for very long deposition times.

Notice that the slope of the linear fit can be used as calibration for the deposition rate of our magnetron sputtering. Using all the data, the deposition rate is 3.175±0.21nm/Wh.

4.3.3. Crystal structure of the iridium thin films

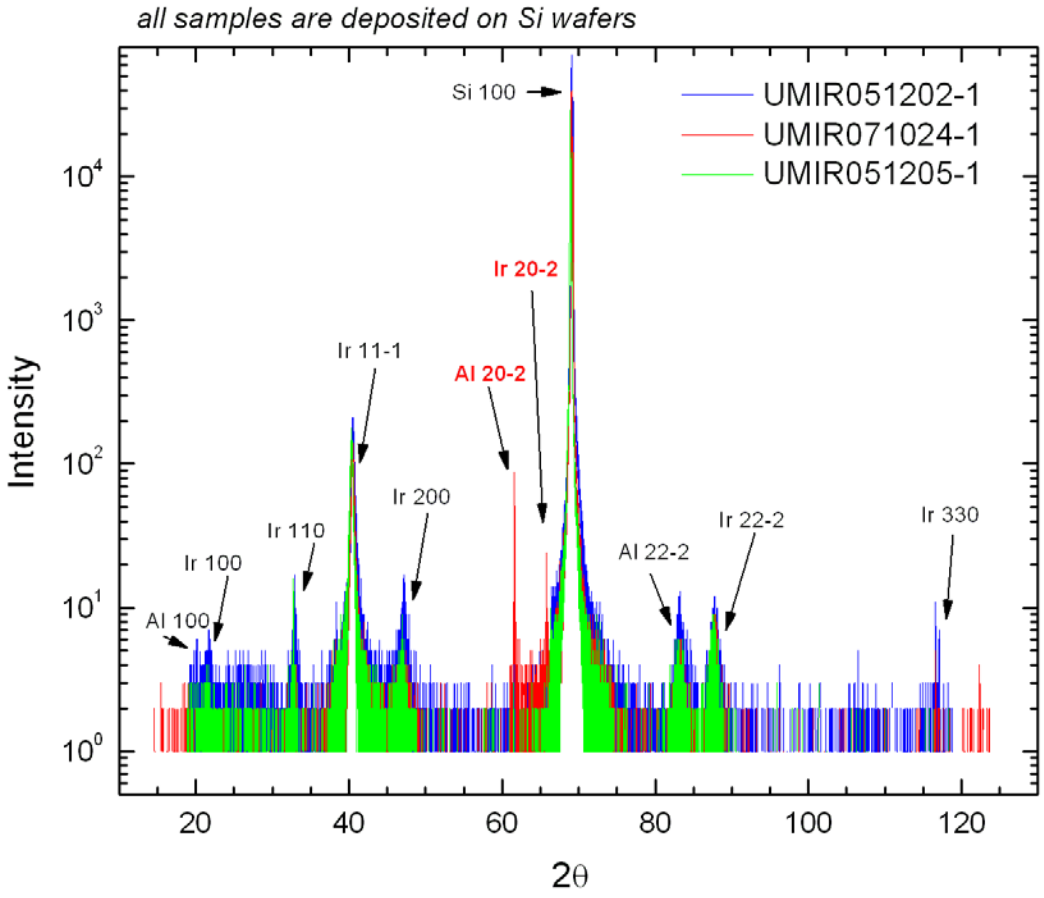

Figure 4.7. The results of 2θ-ω scans for three thin films deposited on Si(100) substrate. Notice the strong peak at the center of the plot corresponding to the Si substrate

To characterize the crystal structure of the films we used the X-ray Diffractometer in a standard 2θ-ω configuration. We identified the primary peaks

via 2θ-ω scans, the samples are consistent with each other, both over the time and for different thicknesses of the iridium films, see Figure 4.7.

The optimization of the scans is done with reference to the Si peak at 69 deg. After we identified all the observed peaks, we only see Ir and two aluminum peaks: Al(20-2) and Al(22-2) for the adhesion substrate. We do not see any iridium silicide peaks which indicate that there is no diffusion at the interface. between the substrate and the thin film. Previous work has shown clear evidence of an iridium silicide layer in samples deposited using Pulsed Laser Deposition, both at the University of Miami and University of Genoa, Italy, however, the Al adhesion layer seems to block the diffusion between Ir and Si.

We also used the width of the diffraction peaks to estimate the crystal size of our samples. The crystal size can be estimated using Scherrer formula: $\delta = \lambda/(\Delta 2\theta)cos\theta$,where δ is the average crystal size, λ is the X-ray wavelength, 2θ is the XRD peak position and $\Delta 2\theta$ is the peak FWHM. For our thin films the crystal size is about 18-20nm. Notice that all our films have been deposited at room temperature.

4.4. Low temperature characterization of the iridium thin films

For the low temperature characterization of the thin iridium films we installed our samples in an adiabatic refrigerator – ADR. Our ADR has a minimum temperature below 50mK and its performance has been characterized as a part of a previous PhD thesis in our group [39]. The samples are mounted

on the cold plate of the refrigerator and in total we can load about 10 samples per run each with four wire outputs. For measuring the transition temperature we use a four wire probe technique. The samples are connected using Al bonding wires. Our bonding wires are 99% Al; 1% Si, with a diameter of 0.001" a elongation of 1-4% and a tensile strength of 15-18g manufactured by CustomChip Connections. We use a manual bonder with a 60 deg. feed for the bonding wire manufactured by Marpet Enterprises MEI. The samples are further connected on the coldplate with Nb/Cu clad wires.

The bias current used to measure the transitions for most of the tests was between 10^{-5}A and 10^{-6}A. In general, for the results reported in this chapter, we consider the transition temperature T_C to be half way on the transition curve, and we fit the derivative of the resistance vs. temperature, dR/dT, between 10% and 85-90% of the transition.

4.4.1. Reproducibility of the transition temperature and dependence on thickness

We have measured the transition temperature for samples with thicknesses in a wide range. In order to keep a general consistency of all our data we patterned all samples and measured for each thickness a sample with the same area 800×1600μm. All the samples were bonded in the same way with 4 Al 0.001" wires from the 4 corners. A complete summary of our data as transition temperature dependence of the thickness is presented in Figures 4.8.

Figure 4.9 shows the same data of Fig. 4.8, zoomed to the low thickness portion of the plot.

It is very important to notice that all the blue points are deposited using our standard recipe, which includes a 2 minute deposition of aluminum as an adhesion layer with a thickness of about 30Å. The depositions of the iridium vary both in duration and R.F. power. The red points in the Figure 4.8. are deposited without the adhesion layer because for very thin layers, where the thickness of Al and Ir become comparable, we want to make sure that the thin film will not behave as a bilayers. Notice that for very thin films (below 100nm) the adhesion between Si(100) and Ir is good without the need for the adhesion layer.

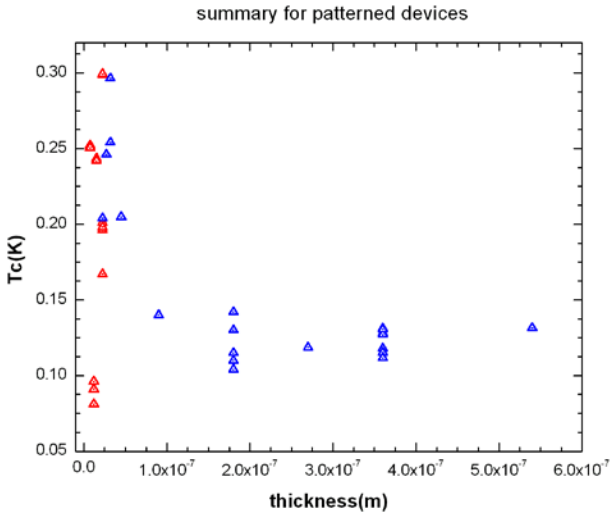

. Figure 4.8. Summary of the thickness dependence for the transition temperature

From Figures 4.8 and 4.9 it seems clear that, for thick film (above ~200 nm), the transition temperature does not significantly depend on the thickness and approaches the bulk value of 113 mK. As the thickness decreases, however,

the transition temperature first increases, reaching a peak value of about 300 mK around 30 nm, then it decreases to zero for zero thickness.

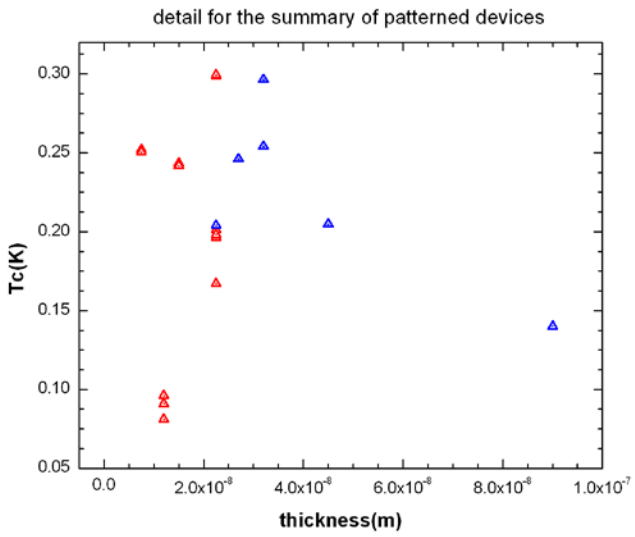

Figure 4.9. Dependence of the transition temperature on the thickness for very thin films

In recent years a lot of attention has been given to the study of Ginsburg-Landau GL approach to critical phenomena [49]. A strong dependence of the transition temperature as a function of the thickness of a superconducting materials has been observed and recently studied in details for many materials, e.g. Al, [50] and Nb [51], [53].

The increase of critical temperature at small thickness was also observed in the 60s, e.g., McMillan (1968) [52]. McMillan et al. explain the increase in critical temperature as a stronger phonon mediated electron-electron coupling due to a softer phonon spectrum (since the film is thinner the frequencies available for vibration for the phonons are smaller and the electron-phonon system becomes stronger coupled).

The thickness dependence of critical temperature from McMillan can be written as:

$$T_C = T_0 + Ae^{-t/t_0} \qquad 4.3.$$

Another interpretation can be derived from the approach by Linhares, who considers that the special boundaries of the thin films are inducing a phase transition. In general critical phenomena arise due to a diverging correlation length of the fluctuations of the "order parameter". In our case we are at the phase transition between the superconducting state and the normal state. As mentioned above a similar first order transition behavior has been observed for aluminum films, on the other hand for niobium thin films a second order phase transition has been reported [52].

The variation of the transition temperature with the thickness can be explained as a limit result if we apply the GL theory to critical phenomena in superconductors. The existence of a phase transition is plausible if we consider the behavior of field theories as a function of spatial boundaries, [49].

If we apply the G.L. theory to a confined slab (infinite sheet of constant thickness) – which is a good approximation for a thin film we can write an analytical dependence of the transition temperature versus thickness as found by Linhares [50]:

$$T_C(t) = T_0 - \frac{A}{t} ln\left(1 - e^{-t/t_0}\right) + \frac{B}{t^2} ln\left(1 - e^{-t/t_0}\right) \qquad 4.4.$$

where T_0 is the bulk transition temperature, t is the thickness of the film, and A and t_0 are parameters related to the superconducting properties of the material.

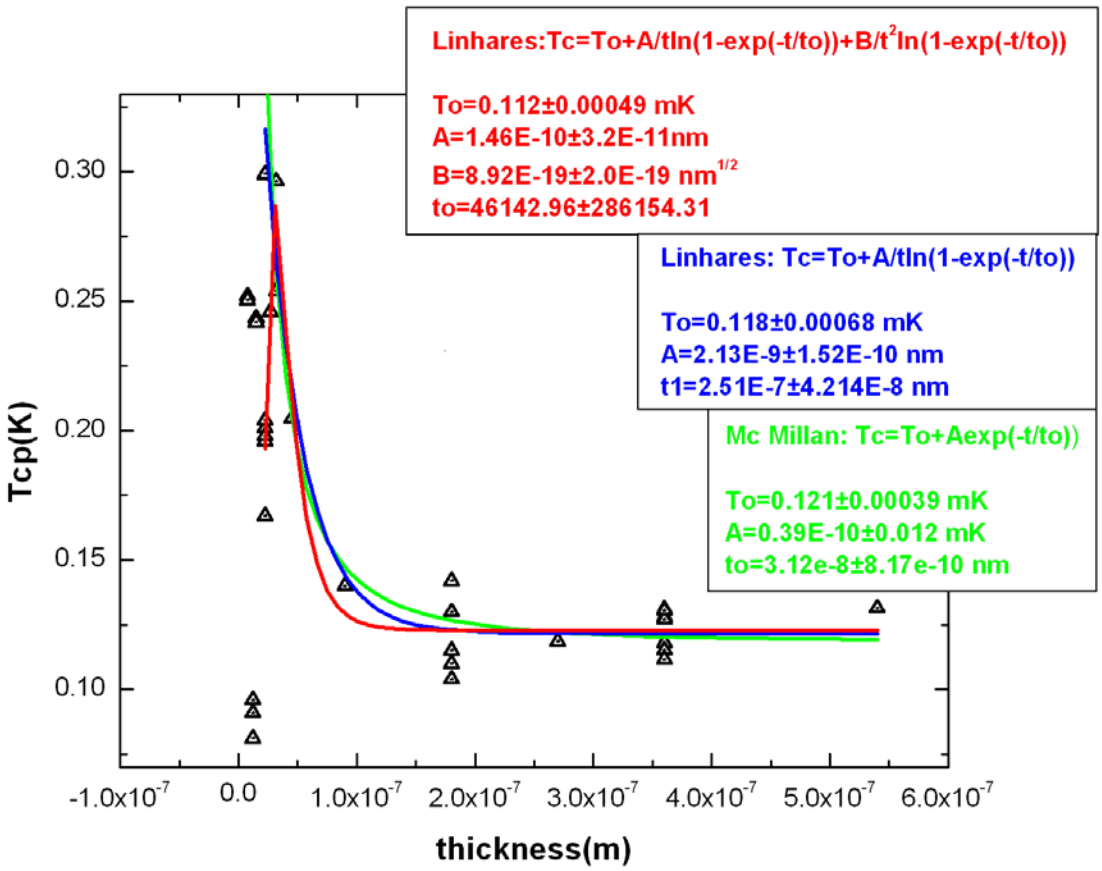

Figure 4.10. First order approximation for the transition temperature dependence on thickness, notice that both models fit almost identical.

Equation 4.4 explains not only the increase in transition temperature, but also its decrease for very small thickness. Equation 4.4 is equivalent to 4.3 if we are interested only on the increase in T_c, in which case it can be expressed as:

$$T_C(t) = T_0 - \frac{A}{t} ln\left(1 - e^{-t/t_0}\right) \qquad 4.4b.$$

Figure 4.10 shows the same data of Figures 4.8 and 4.9 fitted with Equations 4.3, 4.4, and 4.4b. The curve fit quite well the experimental data. As pointed out, the fits using Equations 4.3 and 4.4b are equivalent and properly account for the

increase in transition temperature at low thickness, while Equation 4.4 also accounts for the rapid drop of transition temperature below 30 nm.

4.4.2. Uniformity of the transition temperature

Critical aspects in the fabrication of arrays of microcalorimeters are the reproducibility of the film characteristics, discussed in the previous section and their uniformity over sufficiently large areas.

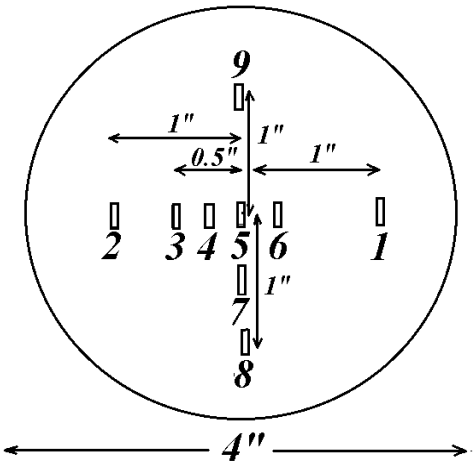

Sample	ΔT (mK)
4	-1.5
5	0
6	1.5
7	-0.4
8	-2
9	-1.8

Figure 4.11. Differences in the transition temperature between samples extracted from different parts of a 4 inch diameter wafer. The temperature difference between devices is smaller than the change in a single device due to changes in the magnetic field trapped in the sample space.

To test the uniformity of the film characteristics over large areas, we deposited Ir on a 4” diameter wafer, and compared the transition temperature between samples distributed over the whole wafer. Figure 4.11. shows the first uniformity test, where we deposited an unpatterned uniform layer of iridium and we cut the samples using diamond disk. We found that the transition temperature

was within 2 mK for samples up to 2 inch apart. This difference is within the experimental error caused by the presence of residual magnetic field in the experimental space.

We repeated the uniformity test over a four inch wafer using patterned devices. We measured the transition of samples of rectangular shape and same area 800μm width and 1600 μm length. All the samples were bonded with 25 μm diameter Al wires at the four corners of the rectangle. The four wire measurements are done at two bias currents 10^{-6}A and 10^{-5}A. The Figures 4.12. and 4.13. show a summary for a current bias of 10^{-6}A. The two large samples where deposited with the following parameters. The sample UMIR080625-1 (Figure 4.12.) was deposited at a RF power of 30W, at argon pressure of 5mtorr for a total time of 4 hours. The sample UMIR080616-2 was deposited at the same RF power and argon pressure but for a total time of 2 hours and is expected to have roughly half the thickness.

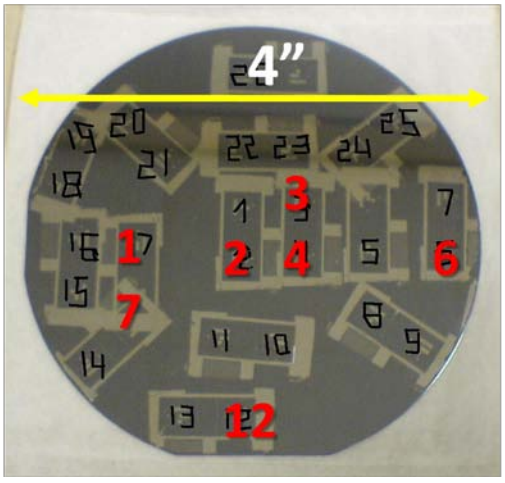

Figure 4.12. a - the position of the measured samples within the wafer

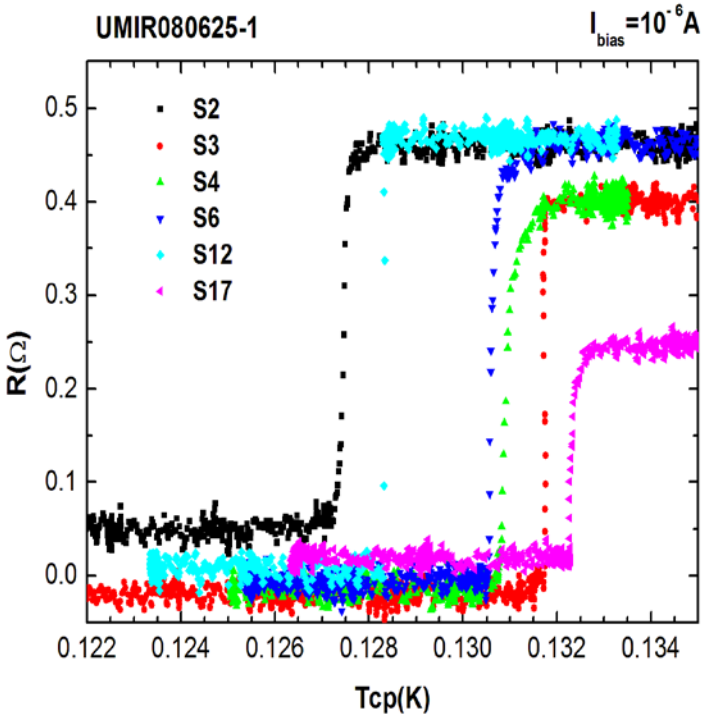

Figure 4.12. b – the position of the measured samples within the wafer

In the Figures 4.12b and 4.13b. we present the results for the transition temperature measurements of samples positioned at different points on the wafer as shown in Figures 4.11.a and 4.11.b.

The samples from Figure 4.11.b have thickness of about 360 nm and the transition temperature is very close between samples, varying by a maximum of about 4 mK over the whole wafer. This is a significant result, as the spread is very small for most TES applications. Moreover, the real spread may be even smaller. Notice, in fact, that samples 2 and 3, while very close to each other, have their transition temperatures 4 mK apart. This seems to indicate that the spread may be due to experimental uncertainties rather than being real. As we

mentioned before, there is a residual magnetic field at the sample location that may vary between measurements due to the ADR parameters. This magnetic field is probably responsible for part of the spread in the transition temperatures. Another explanation for the spread in transition temperature is a small difference in the sample thickness due to the manufacturing process. We have shown before that the transition temperature depends on the sample thickness. Therefore small changes in the thickness between samples is expected to contribute to the spread in critical temperatures.

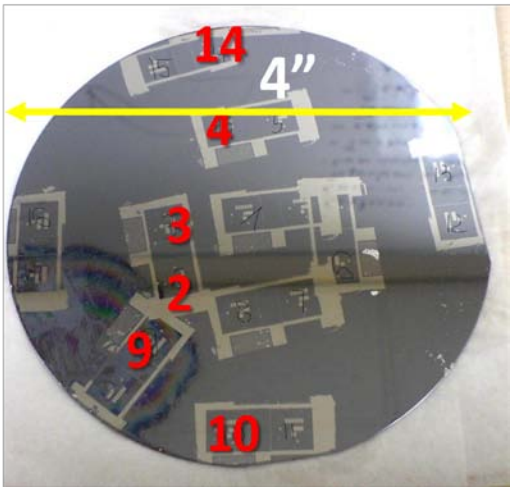

Figure 4.13. a – the position of the measured samples within the wafer for the second test on a thinner deposition

We repeated the same uniformity test using a patterned 4 inch wafer but with thinner iridium (half thickness due to half deposition time, or about 180 nm) and the results are shown in Figure 4.12. b. We observe again similar transition curves between the various samples, however this time the spread in the transition temperature over the 4 inch wafer is a bit larger, about 8 mK. This seems to strengthen the hypothesis that changes in thickness are responsible for

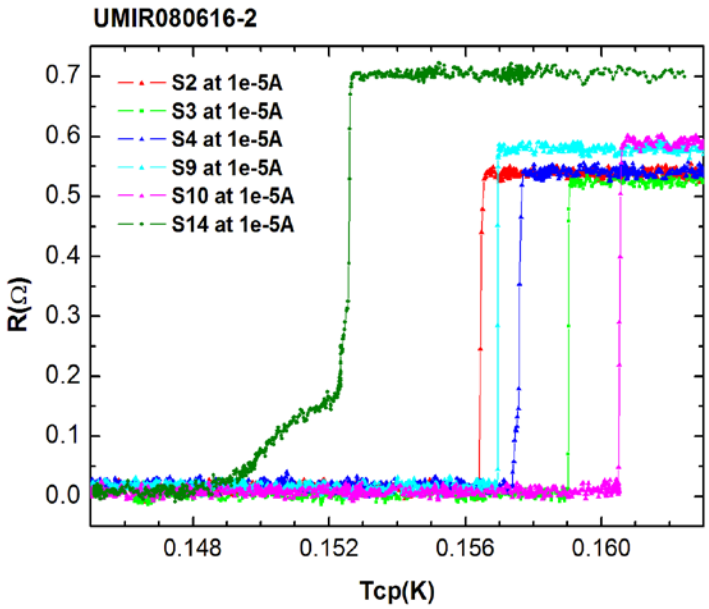

Figure 4.13. b - transition temperature uniformity test over a patterned wafer

the spread in transition temperature. Sample UMIR080616-2 is thinner than UMIR080625-1 and, in fact, has a higher transition temperature, as discussed before. This also means that sample UMIR080616-2 is in a thickness range were the transition temperature is more sensitive to changes in thickness. Assuming that the fractional changes in thickness between the two samples are comparable (the manufacturing recipe is the same), we may expect a stronger effect on the thinner film.

Most important for our application is the fact that the total spread in the transition temperature across the whol wafer is small 4-8mK. Moreover, for future fabrication we know that the spread in transition temperatures across the wafer is inversely related to the film thickness.

Overall our tests are consistent with each other the transitions are very narrow at the working point and consequently a very high sensitivity α, which makes them well suited for use as TESs.

4.4.3. Iridium sensitivity to bias current

We investigated the transition in Ir films with bias current in a wide range between 0.28 μA and 250 μA, Figure 4.14., and we measured the sensitivity α, as defined in the equation 3.1. For the data reported in this section the transition temperature and resistance are measured at the middle point of the transition. For the sensitivity α the value of dR/dT comes from a fit between 10% and 90% of the transition. We found values of α ranging from 200 to 600, depending on the film and the current used.

We also calculated the residual resistivity ratio (RRR) as the ratio between the resistance at room temperature and at 4.2K. We measured the resistance using a standard four wire measurement. The value of RRR varied from 1.5 to 3, depending on the sample. Notice that for the highest value of bias current the transition looks particularly sharp due to self heating of the sample.

Figure 4.15. presents a summary of the dependence of the critical temperature on bias current for one of our sample (UMIR060113-1).

Applying Landau-Ginsburg theory to a thin film we can express the critical current density as:

$$J_C = 2e\psi_\infty^2 \frac{2}{3}\left(\frac{2}{3}\frac{|\alpha|}{m^*}\right)^{1/2} = \frac{cH_C(T)}{3\sqrt{6}\pi\lambda(T)} \propto (1-t)^{3/2} \qquad 4.5.$$

where the second part of the equation 4.3. is expressed in terms of operationally significant quantities and the last part (the proportionality) is valid neat the critical temperature. H_C is the critical field; λ is the penetration depth in the thin film. which depends of temperature as: $\frac{\lambda(T)}{\lambda(0)} = \frac{1}{\left[1-(T/T_C)^4\right]^{1/2}}$; $t = T/T_C$; T_C is the critical temperature.

Form the above equation we can derive an expression for the temperature dependence of the current. We are assuming that the thin film is in zero external magnetic field and the critical H_C will be due to the electrical field applied to the sample.

$$T = T_0\left(1-\left(\frac{I}{I_0}\right)^{2/3}\right) \qquad 4.6.$$

where T_0 is the zero-current critical temperature and I_0 the zero-temperature critical current. Our data fit quite well Eq. 4.4. From the fit of this sample we obtain T_0=120.6 mK and I_0= 440 μA.

As discussed in chapter 3, a critical parameter for the performance of microcalorimeters is the sensitivity $\alpha = \frac{T}{R}\frac{dR}{dT}$. As we can see from Figure 4.13. in addition to the critical temperature, the width of the transition is also changed by the bias current. This can be explained by the power dissipated in the film that affects the state change between superconducting and normal.

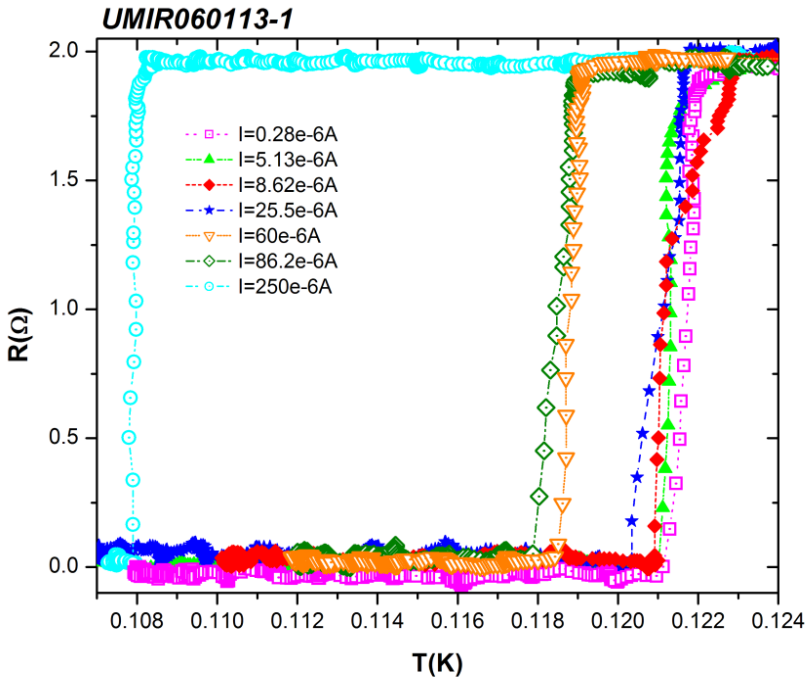

Figure 4.14. Ir film measured at different bias currents between 0.283μA - 250 μA

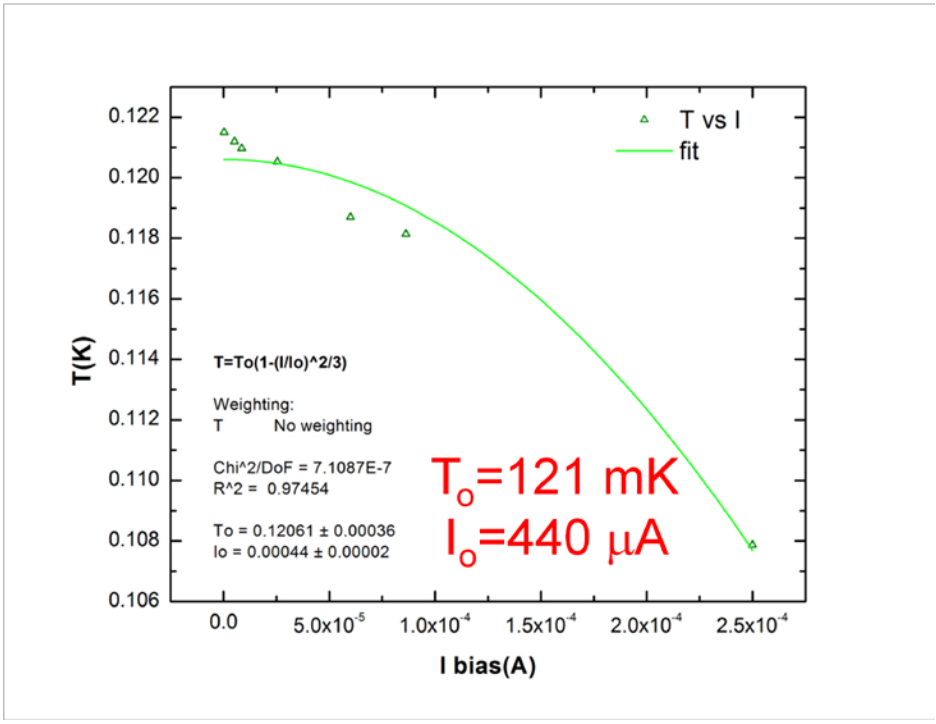

Figure 4.15. Summary for the critical temperature as a function of the bias current.

In previous work done on superconducting thin films for TES detectors, Irwin [40] found a relationship between the critical current for a BCS super conduction film by applying a two fluid transition model to a simple BCS superconductor that behaves in accordance with Ginsburg-Landau theory near the transition temperature by combining the standard GL results for the critical current density and BCS results near the critical temperature for critical field and effective penetration depth. Following Irwin's calculations the resistance reduces to a simple function of temperature:

$$R = R(T) = \frac{V}{c_I I_C(T) + V/c_R R_n} \qquad 4.7.$$

Where I_C is the critical current, V is the bias voltage, R_n is the normal resistance, and c_I and c_R are proportionality coefficients.

Replacing this expression of R in the definition of alpha and assuming that the film temperature is close to the transition temperature so we can use the G.L. critical current shown in equation 4.4. we can express the sensitivity as:

$$\alpha = \frac{2}{3}\left[\frac{(c_R R_n - R_0) c_I^2 I_{c0}^2 R_0}{c_R R_n P_0}\right]^{1/3} \qquad 4.8.$$

Where $P_0 = I^2R$ is the Joule power. This can be expressed as a simple function of current as:

$$\alpha = A\left(\frac{I_0}{I}\right)^{2/3} \qquad 4.9.$$

Where I_o is the zero temperature critical current.

We summarize the dependence of the sensitivity to the bias current for the sample presented in Figure 4.14. When trying to fit our results with the sensitivity

dependence of bias as derived by Irwin the results are not very satisfactory; see blue curve of Figure 16.

This is due to the fact that Irwin's expression assumes that the width of the transition is 0 for no bias current. In reality in a superconductor the resistance is a function of temperature, applied current, and applied magnetic field. For the study of our thin films we shield the external magnetic field so we can neglect its influence and we are applying a small electrical current. At low applied field and current, the form of the transition can be influenced by film non-uniformities, magnetic fields, and non-equilibrium effects near the superconducting-normal interfaces. Even if the superconductor is perfectly uniform and negligible current is carried, the transition will have a nonzero width due to phase-slip events induced by thermal fluctuations [44].

To properly fit the sensitivity data we need to account for this intrinsic width of the transition. We do that by introducing an extra term I_1 in Eq. 4.6. which correspond to a "virtual" current representing the current necessary to generate a transition width equal to the intrinsic one.

Equation 4.9 then becomes:

$$\alpha = A\left(\frac{I_0}{I_1+I}\right)^{2/3} \qquad 4.10.$$

When we introduce the term I_1 the fit to our data is greatly improved, see red curve in Figure 4.15. From the fit we obtain a value of the virtual current I_1=7.6e-7$\pm$1.4e-5A. This seems to indicate that a significant fraction of the transition width in our samples is not due to the readout current, but to other

effects and may explain the poor fits by other groups without using the additional term I_1 [45]

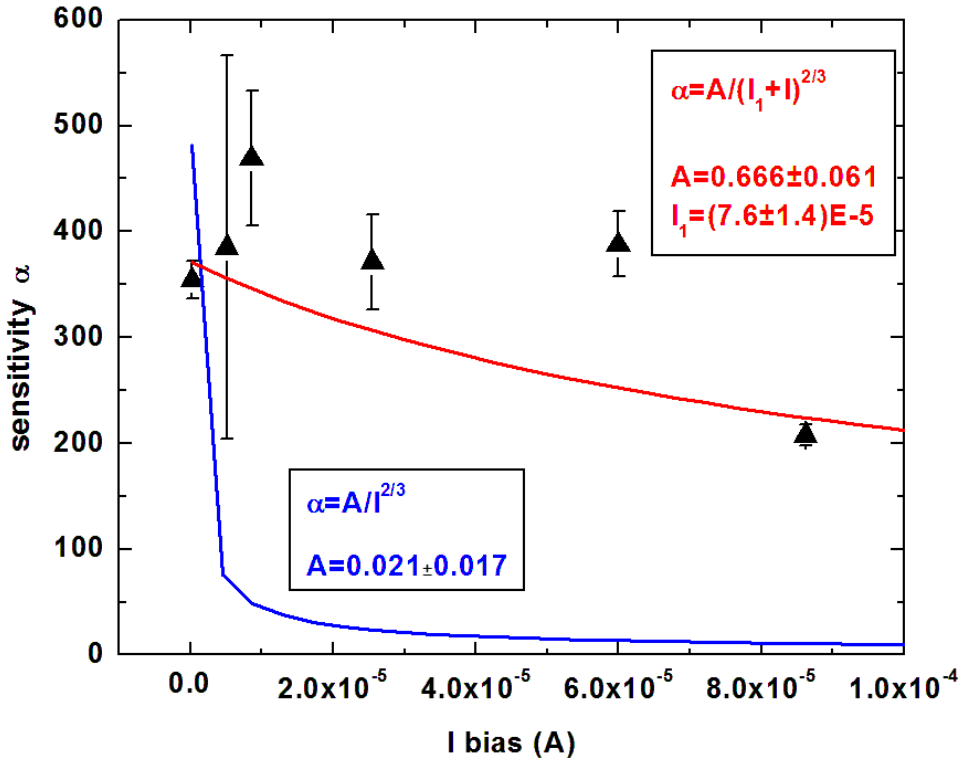

Figure 4.16. The dependence of the sensitivity α on the applied bias current in iridium thin films. Note the that the fit gives us a value for the intrinsic I_1 of 80μA, which accounts for other effects, like a K.T. transition

4.4.4. Critical current dependence on the temperature

To characterize our devices, we also measured the dependence of the critical current density J_C on the sample temperature for values just below the zero current critical temperature. The critical current of the superconducting film imposes a constraint on the maximum Joule power dissipated in a TES and

therefore on the response time of a microcalorimeter (through the electro-thermal feedback).

The results of our critical current measurements are shown in Figure 4.16. Once again, we interpret the results in the framework of the GL theory as presented in the previous paragraph. We expect:

$$J_c = J_0\left(1-\frac{T}{T_0}\right)^{1.5} \qquad 4.11.$$

Notice that Eq. 16 is analogous to Eq. 12. Once again, the data seem to follow closely the GL expression and from the fit we obtain J_0=(1.5503 $\pm$ 0.1248)×10^4 A/cm^2, and T_0=0.11395 $\pm$ 0.0006 K.

In the framework of GL theory we can calculate the critical current density For a bulk iridium J_0 at 0K:

$$J_0 = \frac{cH_c(0)}{3\sqrt{6}\pi\lambda_0} \qquad 4.12.$$

where $H_c(0)$ is the critical magnetic field at 0 K and λ_0 represents the penetration depth.

Using bulk values found in literature for the parameters $H_c(0)$ [46], [47] and λ [46], [48] we obtain an expected zero temperature critical current $J_0 = 3\times10^6\ A/cm^2$, about two orders of magnitudes bigger than our measured value. This result is expected in thin films due to a reduction in the zero current critical fields.

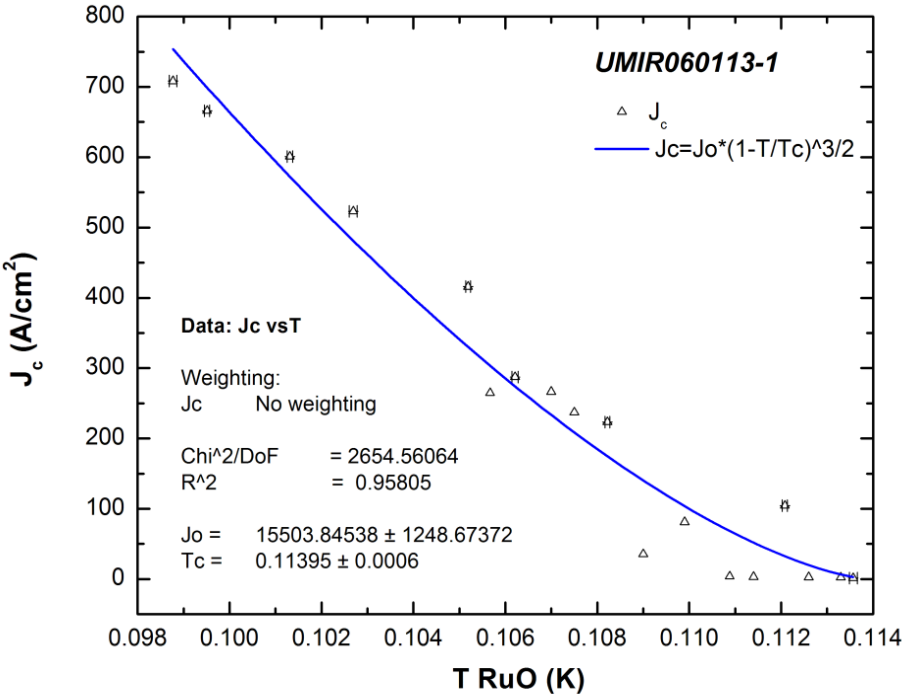

Figure 4.17. The variation of the critical current density on the film temperature.

4.5. Microcalorimeter design

Depending on the type of application the microcalorimeter arrays can be designed using two alternative designs. For example for the MARE1 experiment there is no need for all the detectors to be closed packed together so a discrete design can be used. For radiation detection or dark matter experiments all the detectors need to be on the same wafer/microchip, in the case a fully integrated design is used. The same is true for astrophysical applications, were a close packed array is necessary.

4.5.1. Microcalorimeter discrete design option

This is an older option and it is used when the detectors can be manually asembled. The thin films for the TES is deposited on top of a thin Si(100) mini wafer polished on both sides of the desired size (about $1mm^2$ or less), the absorber is deposited or glued on the back side of the Si wafer. The side with the

TES is then bonded to the bias circuit and the bonding wires (0.001" diameter Al wires) are creating the weak thermal link, see Figure 4.17.

Using this design we succesfully measured the transition of the TES, and aquired X-ray pulses. For testing X-ray detection we used an ^{55}Fe radioactive source with count rate of about 1 photon/second, Figure 4.18.

This microcalorimeter desing is proposed to be used for the MARE1 experiment, were 300 microcalorimeters will be asembled by hand. The microcalorimeters will have an iridium TES and ^{187}Re cristals absorbers as discussed in the second chapter.

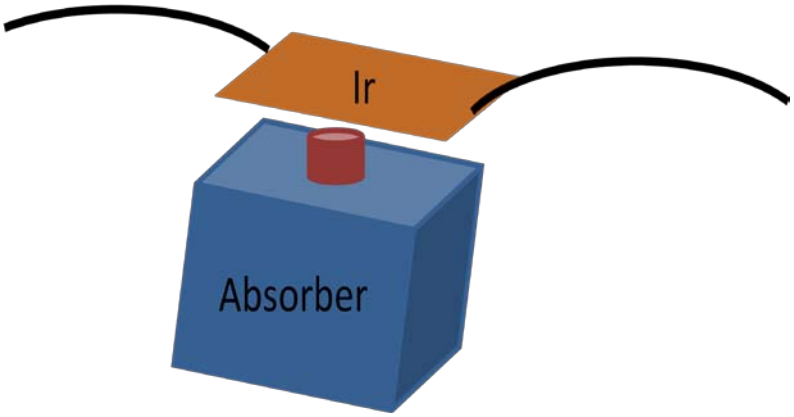

Figure 4.18. Diagram for a microcalorimeter using the first design option

The second stage of the MARE experiment will require a much higher number of detectors thus a fully integrated method will be used.

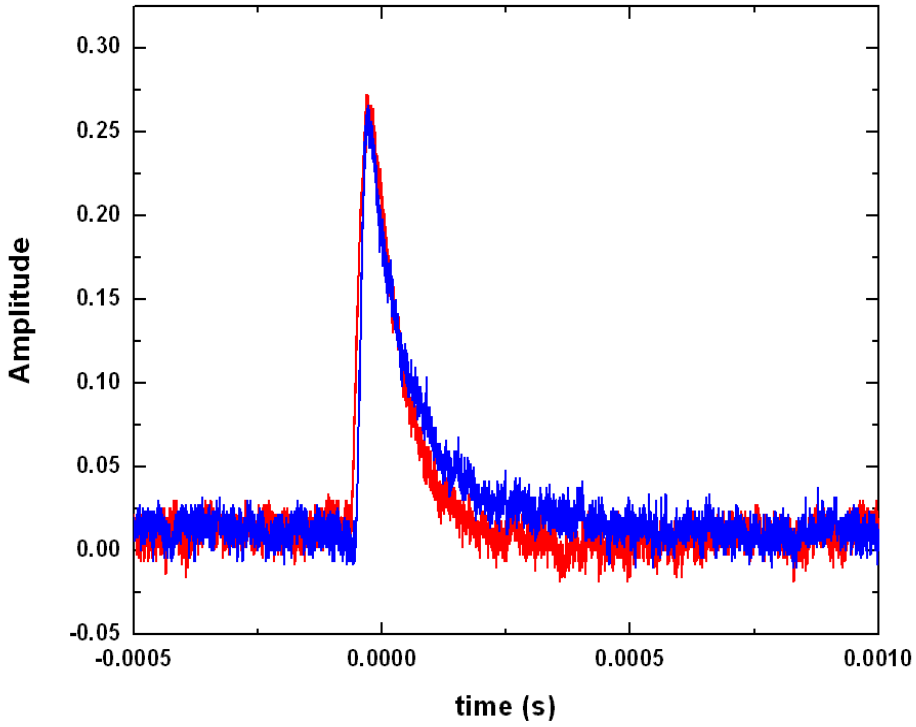

Figure 4.19. X-ray pulse and spectra from a ^{55}Fe source aquired using a X-ray microcalorimeter with Ir TES and Sn abosber (in collaboration with University of Genoa)

4.5.2. Microcalorimeter – fully integrated design

For applications that require close packed arrays of microcalorimeters a fully integrated manufacturing process is required. For example for radiation detection the cross section of a detector will look as presented in Figure 4.19.

Notice that the absorber (shown in green) has a much large area in order to provide a high filling factor. Electrical traces used for biasing the TES will be also covered by the “mushrooms” like structures.

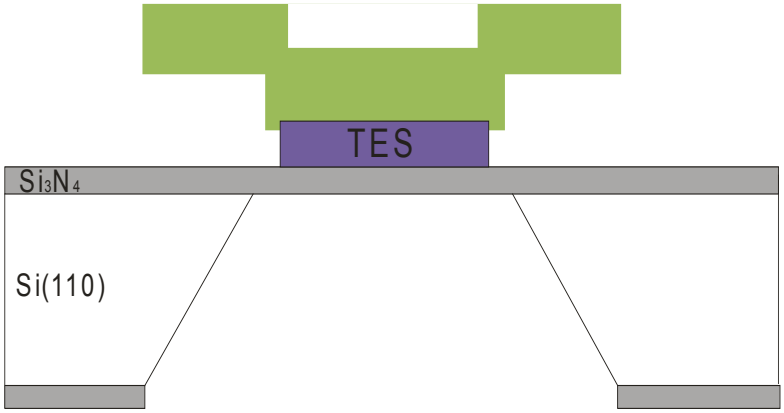

Figure 4.20. Schematic view of a microcalorimeter design with a Sn absorber mushroom like shape, an Ir TES a Si_3N_4 membrane as a thermal link and Si wafer as heat sink. In order to manufacture this microcalorimeter all the steps presented below must be performed.

The manufacturing of such microcalorimeter will require the following steps:

1. Deposition of the patterned TES on a Si(100) wafer with a silicon nitride (Si_3N_4) membrane. In our case the Ir is deposited using a lift-off technique.
2. Deposition of the Al electrical traces that will make the connection between the TES pixel and the readout circuit. The Al patterning will be created using a standard wet-etch photoliotographic patterning. The Al thin layer is covered with photoresist, the desired

pattern is created then the unwanted Al is removed with a chemical etchant.

3. Deposition of a mushroom absorber on top of the TES; the mushroom head will cover the electrical traces so there is a high filling factor for the absorbtion. This step requires two photolotographic steps and will be discussed in detail in paragraph 4.5.2.1.
4. Back etch the Si to suspend the microcalorimeter on the Si_3N_4 membrane. This last step involves the following: cover the microcalorimeter (TES + absorber) with a protective apiezon wax; mask the back side of the Si wafer and etch the Si_3N_4; use the Si_3N_4 to etch the Si underneath the TES; remove the apiezon wax and test the microcalorimeter at low temperature. The etching process will be discussed in paragraph 4.5.2.2.

While we have not built a fully integrated microcalorimeter we have done all the mechanical tests succesfully for each required step.

4.5.2.1. Sn absorber manufacturing

The absorber must be opaque to the incident radiation and have small heat capacity in order to provide a high energy resolution, low heat capacity, high Z materials such as tin (Sn) are therefore best candidates. Tin has been used as an absorber with promising results but the absorber was mechanically cut and

glued on top of the TES [53]. In order to provide a high filling factor for the detector array we are developing a “mushroom” like structure, see Figure 22. In this way the absorber will overhang the TES and will cover the area used for electrical traces. We developed a recipe for deposition of “mushroom” structures for Sn absorbers [54].

The fabrication of the mushroom structure requires the following steps: the cleaned substrate must be photolitographically patterned for the “mushroom stem” structure, the Sn is then deposited and followed by another photolithography step for imprinting the mushroom head. Then the unwanted Sn is removed using wet etching. We are using the same combination of photoresist and developer for the photolithography as in the case of Ir. One issue that we encountered during the mushroom manufacturing was the fact that the photoresist can be burned during the deposition due to the high energy carried by the evaporating Sn. We addressed this issue by reducing the deposition rate of the Sn and by modifying the last step for the photolithography (decreasing the concentration of the developer and increasing the time to remove the photoresist.

The Sn deposition was done in a thermal evaporator with two sources. In order to improve the adhesion between the substrate and the tin we added a thin adhesion film of chromium or titanium. Both had given us good adhesion for thicknesses of Sn up to 2μm.

Figure 4.20. shows the measured heat capacity of an absorber deposited at the University of Miami and measured at the University of Wisconsin. The measured heat capacity is higher than expected from bulk material, primarily due

to the ferromagnetic heat capacity of chromium that was used as an adhesion layer.

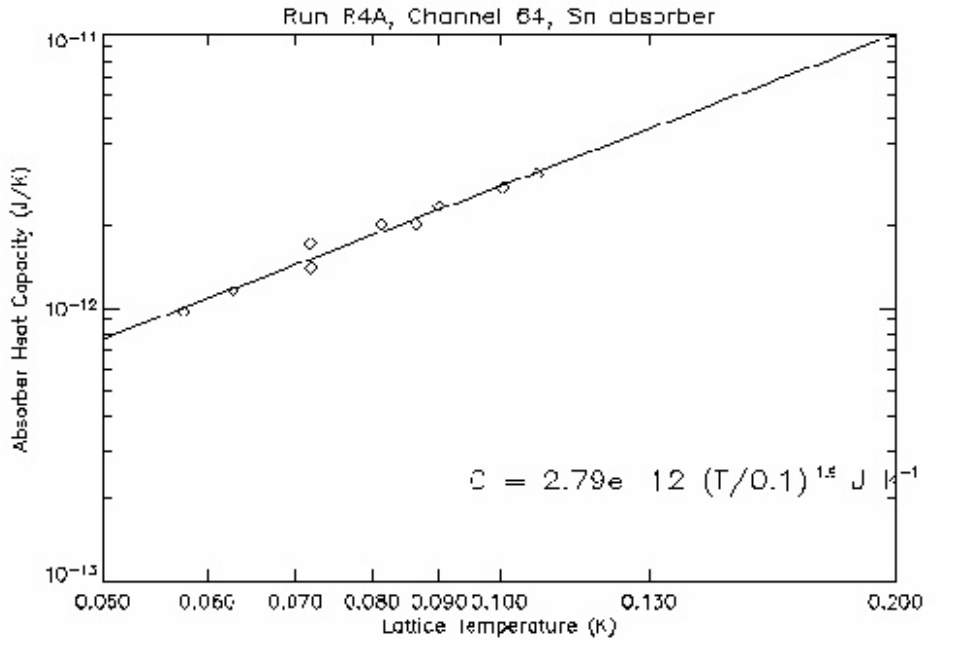

Figure 4.21. Measured heat capacity of a tin absorber

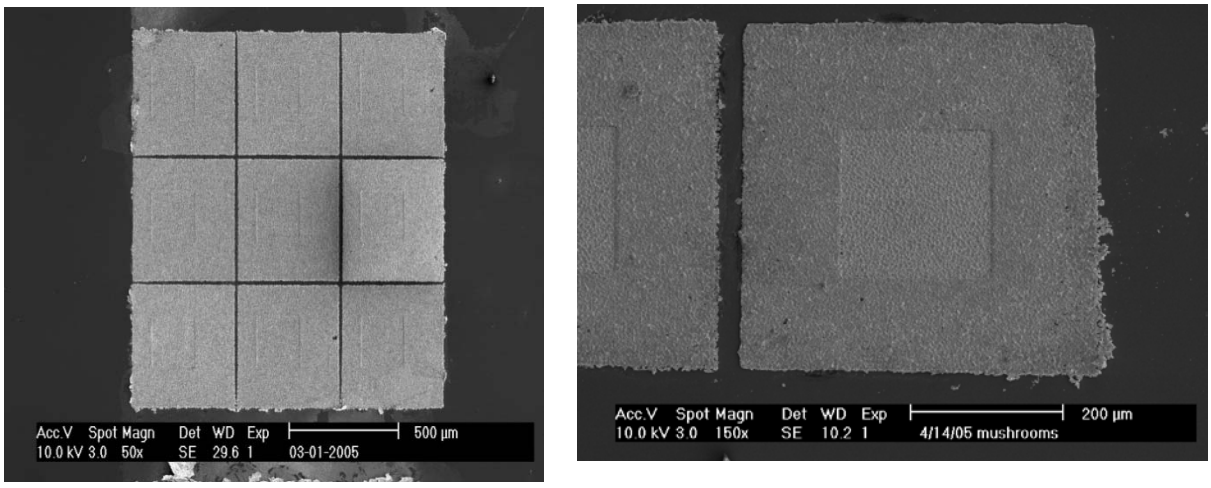

Figure 4.22. a - SEM image of a 3×3 mushroom array with structures of 450×450 μm^2 and stems of 200×200μm^2; b - detail for a mushroom structure

The heat capacity of a Sn thin film of 2mm×2mm×1μm has been measured and is dependent of temperature as a power of 1.5 in the milikelvin range with a value of $2.79e^{-12}(T/0.1)^{1.5}$J/K [55].

For mechanical tests we have also successfully deposited 3×3 mushroom arrays on top of Si(100) substrate, Figure 4.20. We also deposited Sn on top of an Ir TES and did not see any mechanical issues, the adhesion between the two layers was good.

4.5.2.2. Substrate Etching for integrated microcalorimeters

For the substrate etching processes we used wet etching: the Si_3N_4 on the back side of the wafer is etched in correspondence to the position of the TES using 85% hot phosphoric acid (H_3PO_4) at 165ºC [56]. For the next step – the etching of Si we need to take into consideration the fact that we use Si wafers cut parallel with the (100) side. The etching, in fact, is vertical but will have an angle with the horizontal plane of 54.6º. The Si etching was done using 35% potassium hydroxide (KOH) at 80ºC, using the Si_3N_4 as a mask. The main difficulty that we had to overcame was the quality of the Si_3N_4 etching process. It was difficult to find a mask that would survive the harsh hot phosphoric acid. We tried gold (Au) depostion but it does not have a good adhesion and we had to add an extra adhesion layer between the Si_3N_4 and the Au. After several tests we obtained good etching results using Ir thin films deposited via PLD as a mask for the Si_3N_4 , Figure 4.23.

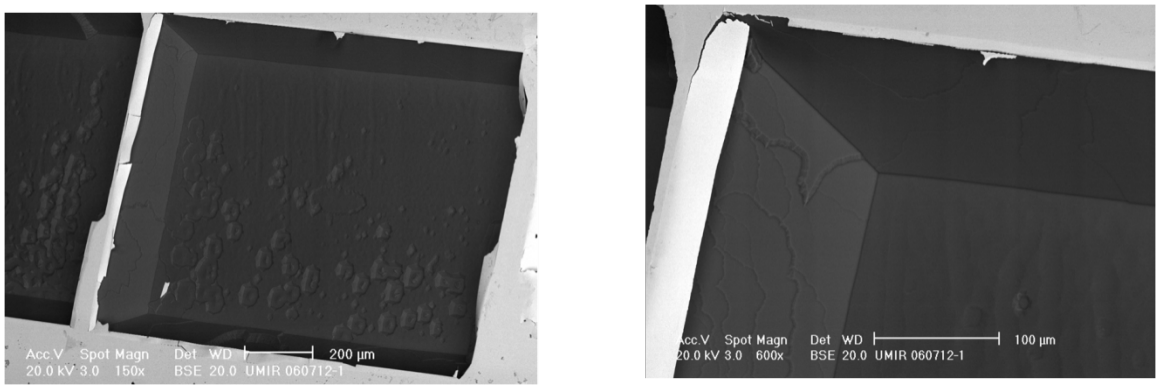

Figure 4.23. SEM image of the etched Si(100), notice the sharp edges due to the crystal structure on the Si , the gray mask is the Ir thin film.

The Ir deposited via PLD has a very good adhesion, survived well to the hot phosphoric acid and was used as a mask. Some minor issues were related with the fact that our PLD facility is not in a clean room enviroment so very small particles of dust or debries that will sit on the Si_3N_4, thus weaken the Ir film and can produce holes in the Si_3N_4 layer.

Chapter 5

5. Alternative bias options for the TES readout

5.1. Background information:

As discussed before, the signal of a TES is usually read out with a SQUID magnetometer used as a current transducer with a low current noise of a few $pA/\sqrt{Hz}$. This option seems to work well for small detector arrays. Due to the fact that every detector in the array will have its own electrical traces towards the SQUID input, the use of a large SQUID array can raise a series of issues like an increase in the base temperature due to overheating through the power lines, also the SQUIDS are dissipating an extra intrinsic power and can overheat the cold plate of the refrigerator. Multiplexing schemes to overcome such shortcomings are being investigated. In collaboration with the University of Genoa our group is proposing two alternative readout options: using high gain transformers and RLC circuits [57].

The use of transformers with high gain in the readout scheme for bolometers is not a totally new idea. Transformers were first used for radiation detection using the first generation of bolometers. However due to the low performance they were not considered for being used to read microcalorimeters. Recent advances in low noise amplifier technology and the capability of making compact high gain transformers makes their use possible. The performance of

the transformers is not as high as the squids but it is possible to use them to detect efficiently the temperature change in the TES with no degradation in performance. Transformers present a series of advantages over the SQUIDs: they do not dissipate power, which makes them a good alternative for a large array bias and they are much cheaper than SQUIDs. The transformers used for the tests presented in this thesis have a gain of 600 and a spin glass core with low magnetic noise and good coupling at mK temperatures. The transformers used are shown in Figure 5.1. and are commercially available from Cambridge Magnetic Refrigeration.

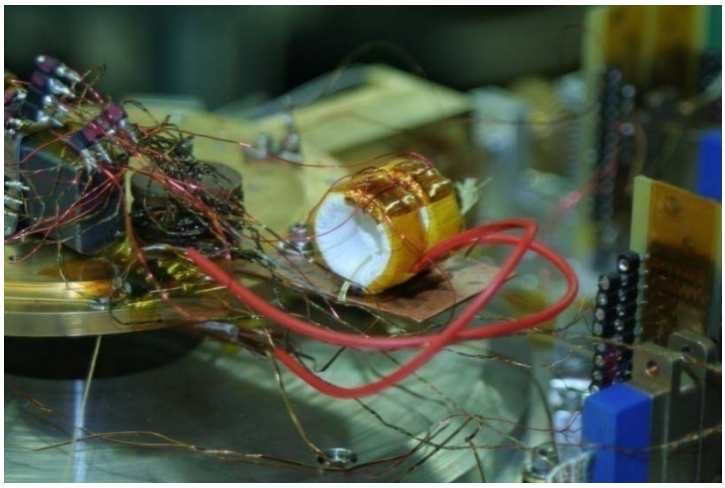

Figure 5.1. Picture of the transformers installed on the ADR cold plate

5.2. Transformers

A typical circuit for the readout of a microcalorimeter with a transformer is shown in Figure 5.2. The equation describing the primary loop is:

$$-V_o + I_p(R + R_L) + L_p \frac{dI_p}{dt} - M \frac{dI_s}{dt} = 0\,, \qquad 5.1.$$

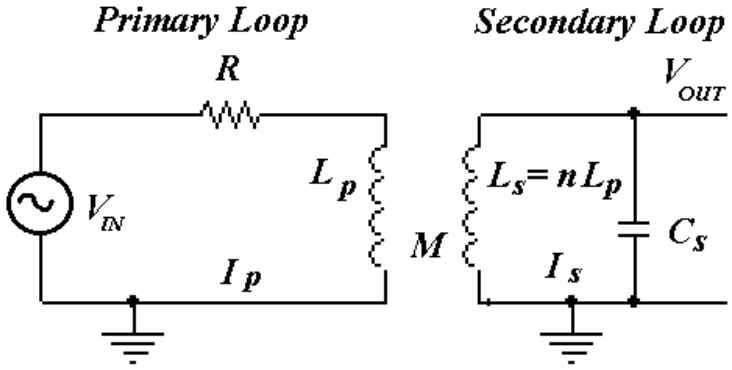

Figure 5.2.Transformer readout scheme

where R is the detector resistance, R_L is a load resistor, I_p, I_s, L_p, and L_s are current and inductor for the primary and secondary loops, and M is the mutual inductance. To evaluate the response to X-rays, we look at small deviations from equilibrium. After removing higher order terms, Eq.20, for small changes from equilibrium, in the frequency domain becomes:

$$\Delta I_p(R_o + R_L) + \frac{V_o}{R_o + R_L}\Delta R + j\omega L_p \Delta I_p - j\omega M \Delta I_s = 0\,, \qquad 5.2.$$

where the symbol Δ indicates small deviations from the equilibrium values.

Similarly we can write the voltage equation for the secondary loop:

$$\frac{1}{C_s}\int I_s(t)dt + L_s \frac{dI_s}{dt} - M \frac{dI_p}{dt} = 0\,, \qquad 5.3.$$

where C_s is the capacitance associated with the coil of the secondary inductor. For small deviations from equilibrium, Eq. 16 becomes:

$$j\omega L_s \Delta I_s + \frac{\Delta I_s}{j\omega C_s} - j\omega M \Delta I_p = 0\,. \qquad 5.4.$$

Combining the above we can express the current in the secondary as:

$$\Delta I_s = \frac{-\omega^2 M C_s V_o}{j\omega L_p (R_o + R_L) + (R_o + R_L)^2 (1 - \omega^2 L_s C_s)} \Delta R \,, \qquad 5.5.$$

where we used the fact that $M = \sqrt{L_p L_s}$. The output voltage is given by:

$$\Delta V_s = \frac{\Delta I_s}{j\omega C_s} = \frac{-j\omega M V_o}{j\omega L_p (R_o + R_L) + (R_o + R_L)^2 (1 - \omega^2 L_s C_s)} \Delta R \,, \qquad 5.6.$$

or

$$\frac{\Delta V_s}{\Delta R} = \frac{j\omega M V_o}{(R_o + R_L)^2 L_s C_s} \frac{1}{\omega_1 \omega_2} \frac{-1}{(1 + j\frac{\omega}{\omega_1})(1 + j\frac{\omega}{\omega_2})} \,, \qquad 5.7.$$

with the corner frequencies given by:

$$\omega_{1,2} = \frac{L_p}{2 L_s C_s (R_o + R_L)} \left(1 \pm \sqrt{1 - \frac{4 L_s C_s (R_o + R_L)^2}{L_p^2}} \right). \qquad 5.8.$$

For $\frac{4 L_s C_s (R_o + R_L)}{L_p^2} << 1$, Eq. 5.8. becomes:

$$\omega_1 = \frac{(R_o + R_L)}{L_p} \text{ And } \omega_2 = \frac{L_p}{L_s C_s (R_o + R_L)} \,. \qquad 5.9.$$

Equation 5.7. represents the transfer function of a band-pass filter with corner frequencies ω_1 and ω_2, see Figure 5.2. We can therefore design our readout scheme to have the detector signal coincident with the interval of maximum gain, where $\omega_1 < \omega < \omega_2$, and the gain of the system is:

$$\left(\frac{\Delta V_s}{\Delta R} \right)_{\max} = \frac{M V_o}{(R_o + R_L) L_p} = \frac{n V_o}{(R_o + R_L)} = n I_{bias} \,, \qquad 5.10.$$

where *n* is the ratio between the numbers of loops in the transformer.

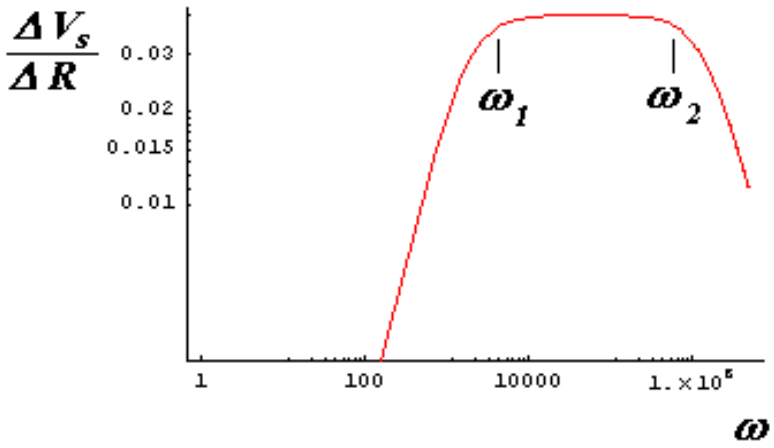

Figure 5.3. Frequency response of a transformer from eq. 5.7 were the corner frequencies are given by equation 5.9

Multiplexing detector arrays simplifies the electrical circuits, and reduces the number of wires to the cold stage. The working principle of transformers makes them natural candidates for frequency multiplexing. The principle is identical to frequency multiplexing in SQUIDs. Multiple detector outputs from the same row of an array can be attached to a single inductor working as secondary loop, as shown in Figure 5.4. Each column is then biased at the same frequency with a single bias line. To reduce crosstalk, capacitors of different capacitance are added in series to the primary loop of each detector circuit. This gives each detector a resonant frequency approximately equal to:

$$\frac{1}{2\pi}\frac{1}{\sqrt{C_p L_p + C_s L_s}}, \qquad 5.11.$$

where C_p is the capacitance of the primary loop added for multiplexing. With C_s, L_s, and L_p the same for all channels, C_p determines the resonant frequency. This is effective until C_pL_p becomes smaller compared to C_sL_s.

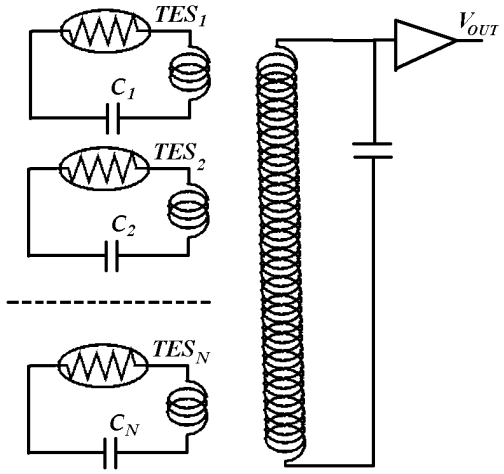

Figure 5.4. Schematic view of the idea for multiplexing TES detectors using transformers

5.3. Preliminary tests and proof of concept

To compare the performance of transformers to our estimates and to demonstrate the application to the readout of microcalorimeters we tested transformers manufactured by Cambridge Magnetic Refrigeration consisting of individual toroidal inductors with 600 turns around a spin-glass core. The inductors have been tested to provide good response at low temperature. The inductors are used as the secondary loop of the transformer while the primary loop is made by simply winding a wire around the toroid.

We first made room temperature preliminary tests using various values for the resistance, as shown in Figure 5.4. We used a transformer with a 600 gain and measured the transfer function using a low noise amplifier with a gain of

21.33 and a standard Stanford amplifier. For different values of the input resistance the width of the transfer function varies as shown in Figure 5.5.

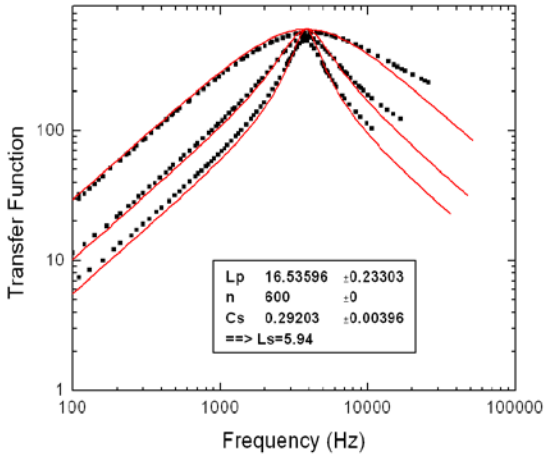

Figure 5.5. Transfer function as a function of frequency for different values of the input resistance *R* (data points), and best fit to the (data lines)

We notice that, as expected, as the resistance is increasing the transfer function becomes narrower. The model fits out data quite well with values of C_s=292 pF, L_p=16.5μH, and $L_s=n^2L_p$=5.94 μH. We also tested the same transformers at 100 mK and found similar behavior, but with inductance values a factor of three lower.

A critical parameter in the implementation of transformer readout is the stray capacitance of the secondary loop. For single channel readout, C_s determines the bandwidth of the electronics through ω_2, while for multiplexing it limits the possible range of resonant frequencies. In our measurements, the value of C_s is a combination of the intrinsic capacitance of the secondary loop (due to the closely spaced 600 turns around the core) and of the wiring and FET amplifiers. To separate the two contributions we used the secondary loop as a

simple inductor in an LR circuit as in Figure 5.6. decoupling the effect of the intrinsic and external capacitance. The result is shown in Figure 5.7. and gives a value for the intrinsic capacitance of 92 pF, a factor of three smaller than the total one. These represent the lower limit of capacitance for these transformers.

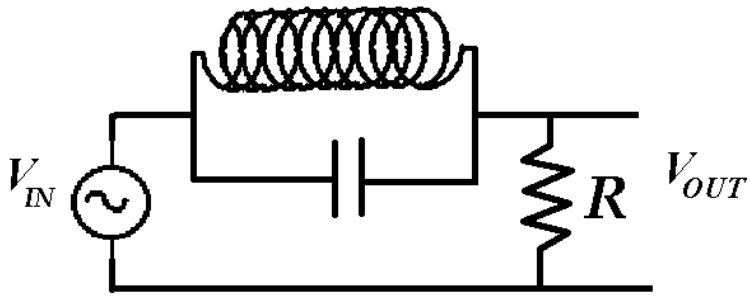

Figure 5.6. Schematic of the circuit used to measure the intrinsic capacitance of the transformer

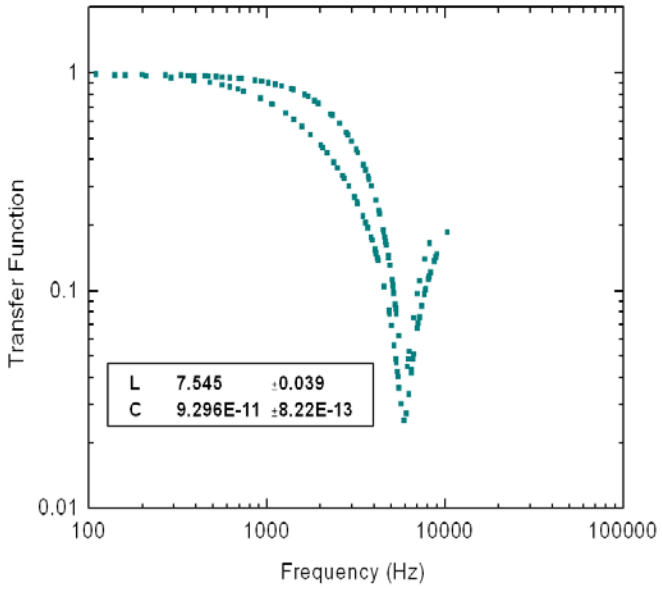

Figure 5.7. Measured transfer function for the transformer, the capacitance, it is a limiting factor in the performance of the detector.

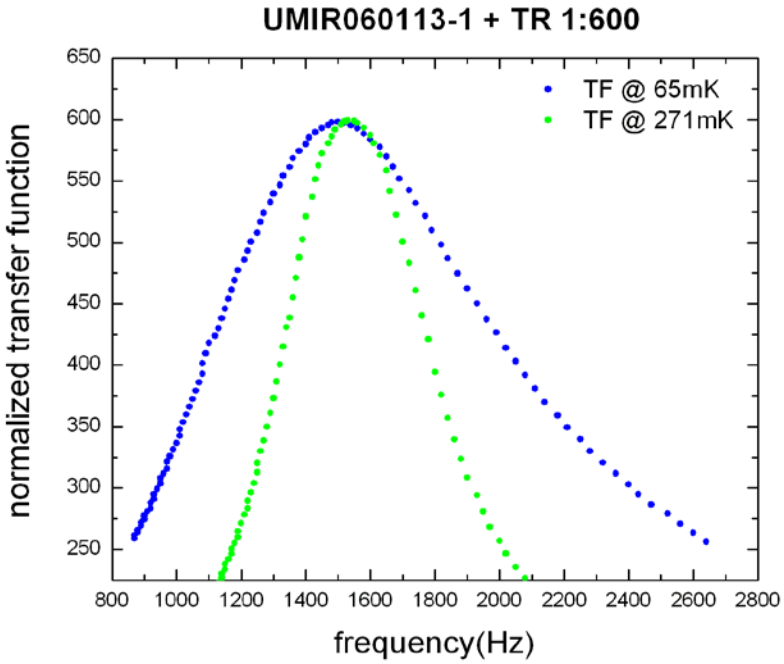

Figure 5.8. TF acquired at temperatures well below the transition temperature - 65mK and above the transition temperature - 271mK

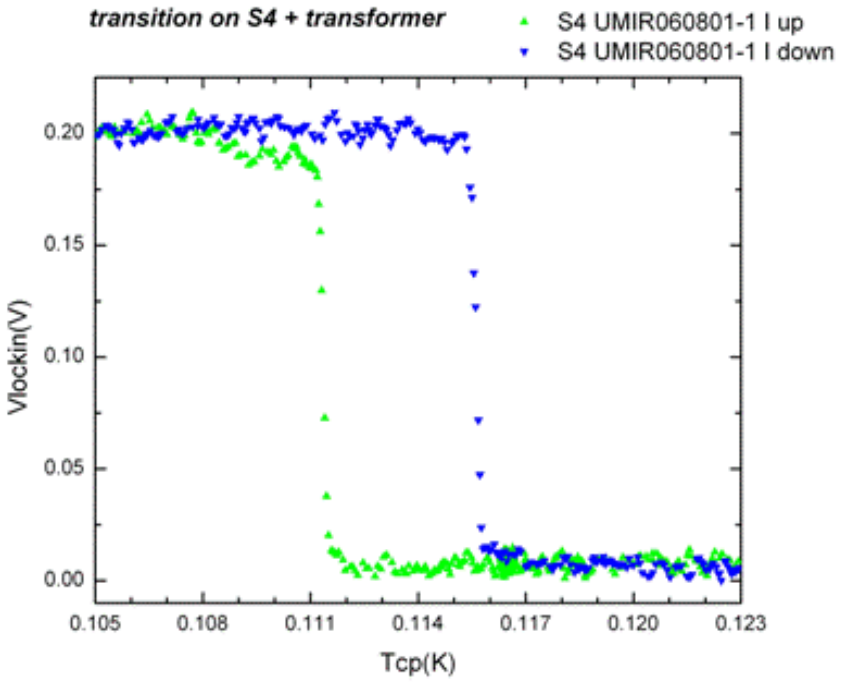

Figure 5.9. Typical transition temperature measured using a transformer readout circuit, the input bias is 1e-6A, we can see clearly a fast change in output due to the increase in temperature around 110mK. The small variation in temperature can be explained by the presence of a small residual magnetic field on the cold plate.

We also coupled an Ir TES to our transformer readout circuit. We measured the transfer function of the circuit above and below the transition temperature, for a thin film deposited at 30W for 2h (Fig. 5.8). We observed a clear difference in the shape of the TF as the resistance of the film decreases. Notice that the resistance does not go completely to zero due to the effect of stray resistance of the wires and joints.

In the Figure 5.9. one can see a typical transformer readout response to a superconducting to normal phase transition of an Ir thin film. The temperature vas varied from about 90mK to about 125mK, to ensure a complete superconducting to normal phase transition. The measurement was obtained by imputing a variable frequency constant voltage signal on the input of the transformer circuit and reading out the output of the transformer, in this case, we used a 1:600 transformer turn ratio. The output of the transformer was further amplified using a low noise amplifier with a 21.33 gain and a standard Stanford SR560 amplifier with a gain of 1000.

As a proof of concept, we tested a microcalorimeter with an Ir TES and a Sn absorber fabricated in our clean room facility; the X-ray and noise acquisition was done with the help of our collaborators at the University of Genoa. We used a transformer to read out the signal from a TES microcalorimeter. A pulse due to a Mn Kα X-ray from a ^{55}Fe source is shown in Figure 5.10. Note that this was a proof of concept and neither the detector nor the electronics were optimized for performance. The pulse has a rise time of 19 μs, corresponding to a bandwidth $\omega_2 = 53\ kHz$.

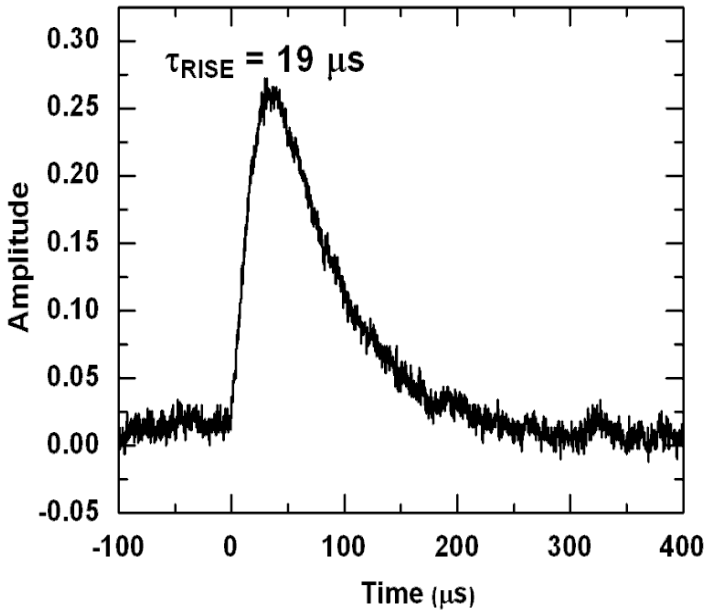

Figure 5.10. Mn Kα pulse for a microcalorimeter composed of an Ir TES and Sn absorber, note that no optimization was used so better resolution can be observed.

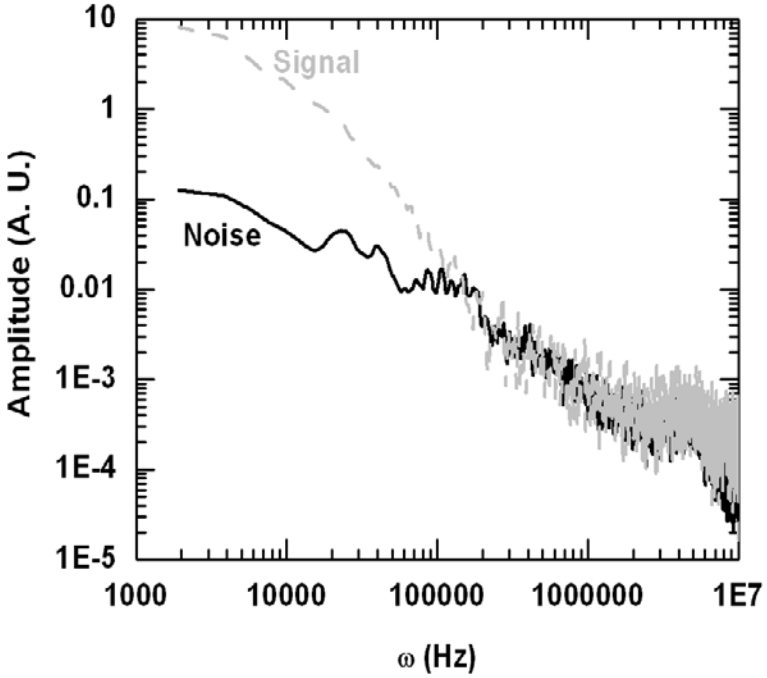

Figure 5.11. FFT of signal and noise for the detector described in previous figure, there is a clear difference between the noise and the signal level ~10:1

Figure 5.10. and 5.11. are showing the pulse and noise spectra in the frequency domain. By fitting the noise spectrum we get a cutoff frequency, due to the transformer system, equal to (57±4) kHz, which is in agreement with the pulse rise time. We used the noise spectrum rather than the pulse spectrum as the pulse is dominated by the much shorter detector time constant. The observed bandwidth is in good agreement with our calculations. Using the values for the transformer parameters previously measured, the value of ω_2 corresponds to a detector resistance of 0.39 Ω, in agreement with similar devices that we have tested. This bandwidth is already sufficiently large for single detector measurements, as it contains the significant detector signal, Figure 5.11. To obtain larger bandwidth, such as for multiplexing, it is necessary to reduce the detector resistance.

5.4. RLC resonant circuits for TES read out

The idea of simplifying the readout circuit can be pushed even farther by using a simple RLC resonance circuit. A diagram of the circuit is shown in the Figure 5.12, where the R is the transition edge sensor (in our case the iridium thin film) the L and C are the inductance and capacitance which must be carefully chosen, the R_W is the resistance of the wires and the C_P the capacitance due to the amplifier, [58].

We can write the equations for the circuit presented in Figure 5.10. and solve for the transfer function

$$V_{in} - Ri_1 - \frac{1}{j\omega C_1}(i_1 - i_2) - j\omega L i_1 = 0 \quad 5.12.$$

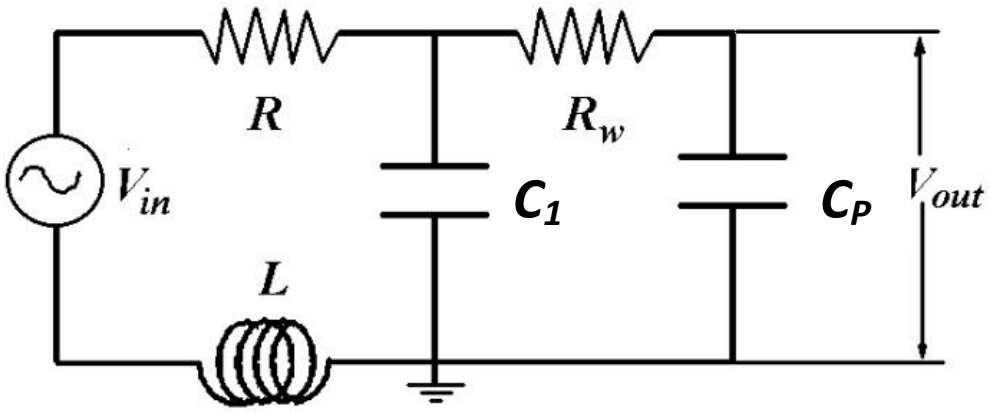

Figure 5.12. Schematic diagram of the RLC bias circuit

$$-\frac{1}{j\omega C_1}(i_2 - i_1) - R_w i_2 - \frac{1}{j\omega C_2} i_2 = 0 \quad 5.13.$$

$$j\omega C_1 V_{in-}(j\omega C_1 R + 1 - \omega^2 L C_1) i_1 + i_2 = 0 \quad 5.14.$$

where the V_{in} is the input voltage, R the TES resistance R_w the resistance of the circuit wires, L the inductance, C the capacitance and C_p=C_2 the capacitance due to the room temperature amplifier.

With the output voltage of ,

$$V_{out} = \frac{i_2}{j\omega C_2} \quad 5.15.$$

If $R_w \gg R$ and $C_1 \gg C_2$, the calculate the transfer function becomes:

$$TF = \left|\frac{V_{out}}{V_{in}}\right| = \frac{C_1}{-C_1 + \omega^2 L C_1^2 - j\omega C_1^2 R - j\omega C_1 C_2 R_w + j\omega^3 L C_1^2 C_2 R_w + \omega^2 C_1 C_2 R R_w}$$

$$TF = \frac{1}{[-1+\omega^2 C_1(L+C_2 R R_w)] - j\omega(C_1 R + C_2 R_w) + j\omega^3 L C_1 C_2 R_w} \quad 5.16.$$

Equation 5.16. represents a resonant circuit with resonant frequency:

$$\omega_0 \approx \frac{1}{\sqrt{LC_1}} \quad 5.17.$$

$$\left|\frac{V_{out}}{V_{in}}\right| = \frac{1}{\frac{1}{\sqrt{LC_1}}\left[C_1 R + C_2 R_w - \frac{LC_1 C_2 R_w}{LC_1}\right]} = \sqrt{\frac{L}{C_1}}\frac{1}{R} \quad 5.18.$$

If the resistor in the circuit is a TES, then the amplitude of the resonant peak depends on 1/R and is a direct estimator of the TES resistance. With the proper values of *R*, *L*, and *C*, the “voltage gain” of the resonant circuit becomes sufficiently large to bring the Johnson noise of the TES above the noise of the amplifier used to read out the signal. It is therefore sufficient to bias the TES in AC at the resonant frequency and demodulate it at room temperature to measure the TES resistance.

We are presenting a simple method for optimizing the parameters of the RLC resonant circuit taking into account the requirements of the experiment.

We begin by summarizing the basic parameters of the resonant circuit performance: the resonant frequency is given by equation 5.17.

$$\omega_0 \approx \frac{1}{\sqrt{LC_1}}$$

the transfer function at the resonance peak - we call it voltage gain is:

$$G = \frac{V_{in}(\omega)}{V_{out}(\omega)} = \frac{1}{R}\sqrt{\frac{L}{C}} \quad 5.19.$$

From simulation we can estimate the bandwidth for the resonator as:

$$\omega_{max} = \frac{2R}{L} \quad 5.20.$$

The Johnson noise of the TES, e_J=sqrt(4k_BRT) behaves like a voltage generator, to achieve best performance we need the noise of the FET amplifier e_{amp} to be smaller than the Johnson noise meaning:

$$TF\sqrt{4k_BRT} = e_{amp} \quad 5.21.$$

Were k_B is the Boltzmann constant, R is the resistance of the TES, and T is the temperature.

Using the results from the equations 5.19. and 5.20. we can predict the upper limit required value for the capacitance for the RLC circuit.

$$C < \frac{4k_BT}{\omega_{max}e_{amp}^2} \quad 5.22.$$

The above equations give just enough information for optimizing the parameters and the performance of the RLC circuit. In particular, for a give experiment we need to take into consideration the following:

1) The value of the TES resistance *R* is determined by the manufacturing process; the signal bandwidth ω_{max} is determined by required detector speed; the amplifier noise e_{amp} is determined by the room temperature amplifier used.

2) Given the experimental constrains just mentioned, it is possible to use equation 5.20. to determine the maximum value ofthe inductance *L* that can be used:

$$L < \frac{2R}{\omega_{max}} \qquad 5.23.$$

3) Equation 5.21. determines the maximum value of the capacitance *C* that can be used.

4) The combination of inductance *L* and capacitance *C* determines, through Eq. 5.17. the resonant frequency of the circuit.

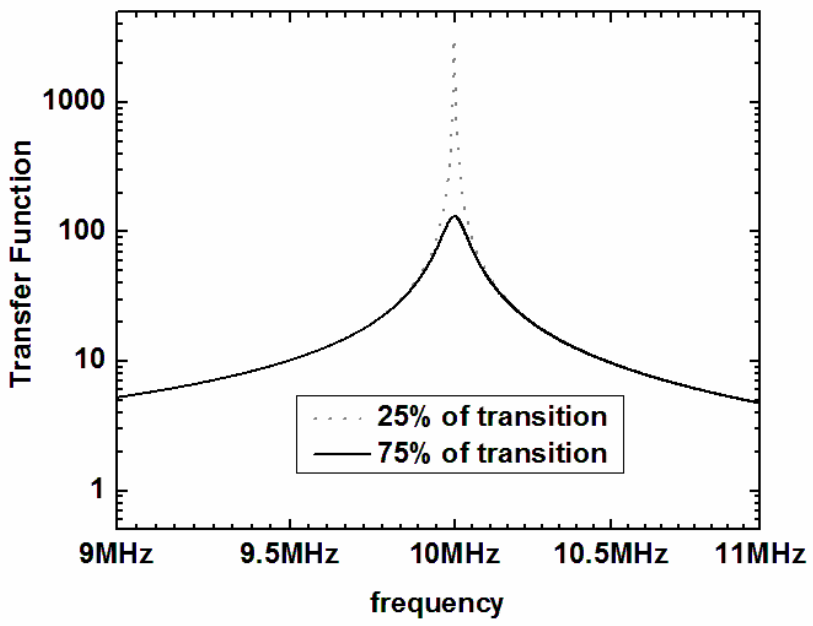

Figure 5.13. Simulated transfer function at 25% of the transition and 75% of the transition for a sample with normal resistance of 0.4 Ohm, L=500nH, C=400pF

As an example, we can assume a TES with normal resistance of 0.4Ω, similar to the Ir TESs fabricated by our group and a resistance at the working

point *R*=50 mΩ, a bandwidth ω_{max}*~100 kH*, necessary for X-ray detection, and a very good amplifier, with $e_{amp} = 0.5\, nV/Hz$

Our simple calculations show that we need a maximum inductance *L=500 nH*, a maximum capacitance *C=400 pF*, and therefore a minimum resonant frequency f_o*=10 MHz*.

The resonator transfer function at 25% and 75% of the TES normal for the mentioned parameters are shown if Figure 5.11. As this example shows, we expect this scheme to work best for X-ray detectors in the frequency range of *10-100 MHz*, a range where it is still possible to use FET amplifiers. For slower detectors the resonance frequency can be lowered.

As a proof of concept we tested a couple of inductance and capacitors, using commercial discrete components, we designed our circuits such that the resonance frequency was between 80kHz and 300kHz. In the figure 5.14. we present the transfer function measured above and below the transition temperature using a typical iridium thin film deposited at an RF power of 30W and argon pressure of 5 mtorr of 2 hours.

The value of the transfer function at the resonant peak clearly changes when the film resistance changes, although the amplitude of the resonant peak, especially below the transition, is limited by a parasitic resistance in the circuit due to the commercial inductor and capacitor used. The inductors used were of 500mH and have an intrinsic resistance of about 100mOhm which is quite significant for our application. To improve the transfer function response above and below the transition a fully superconducting circuit will be necessary.

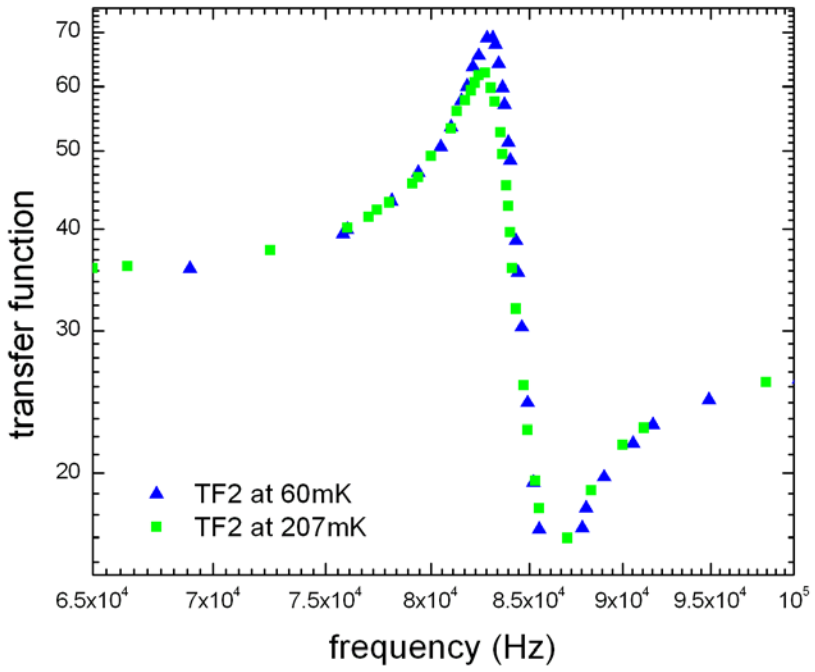

Figure 5.14. Measured transfer function above and below the transition temperature, the performance was limited by the commercial L and C used, L=1mH, C=3.9nF

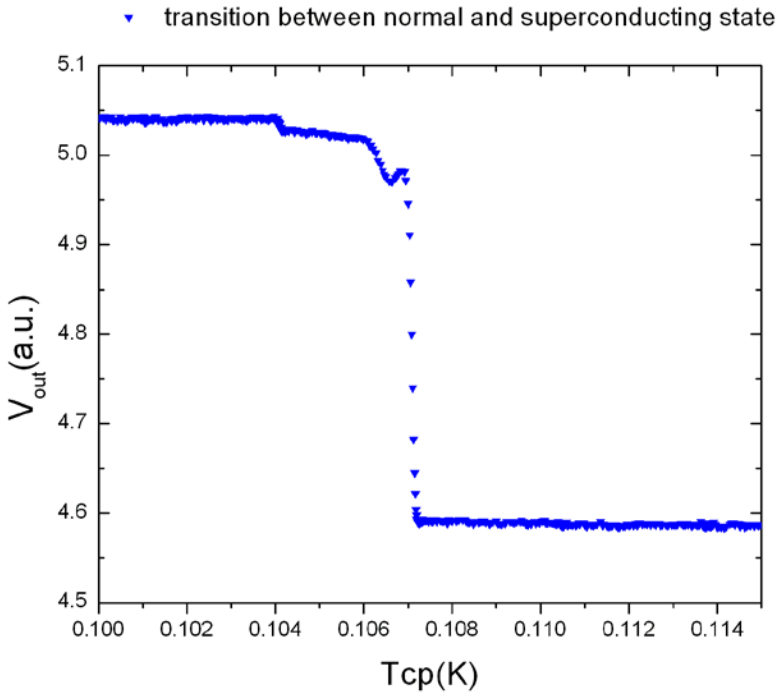

Figure 5.15. Transition on an Ir thin film UMIR060801-1 measured using a RLC circuit biased at the resonant frequency,

We also measured the film transition by biasing the circuit at the resonant frequency. In Figure 5.15. we present a typical transition temperature acquired using an RLC resonant circuit.

Notice that the figure is reversed compared to traditional transition curves as we decided to represent on the y-axis the output voltage, which depends on 1/R. The finite value of V_{out} below the transition is due, again, to the residual resistance in the inductor that we already discussed.

Chapter 6

6. Conclusions and perspectives

For this work we characterized the superconducting iridium thin films from the point of view of reproducibility, uniformity response to critical current, bias and thickness. Knowing the response of the thin film to all these parameters we are able to optimize the recipe for a transition edge sensor using a single layer superconducting iridium suitable for future experiments as MARE I and II and next generations of dark matter cryogenic microcalorimeter detectors.

We are also proposing two alternative options to the SQUID readout circuit; we show that they can be used for most detector readout applications but further work can be done to optimize the sensitivity in signal acquiring. In particular we show that both alternative options aver viable for reading out X-ray signals below 10keV with good sensitivity.

We investigated the use of transformers add RLC resonant circuit for biasing transition edge sensor detectors. We had shown that these alternatives provide a competitive low cost and low power alternative to SQUIDS even though their performance will be somewhat lower. An RLC resonant bias circuit can be integrated with the TES detectors and if superconducting materials are used for the inductors and capacitors, there will be no heating loses, and can be used for large detector arrays.

References:

Chapter 2:

1. Proceedings of the 12th int. Workshop on Low Temperature Detectors (LTD12) J. of Low Temp. Phys. 151, ½ 2008.

2. S.P. Langley, in Proceedings of the American Academy of Arts and Sciences XVI (1881).

3. P. Curie, A. Laborde, Compt. Rend. 136, 673 (1903).

4. F. Simon, Nature 135, 763 (1935).

5. D. Andrews, R.Fowler, M. Williams, Phys. Rev. 76, 154 (1949).

6. S.H. Moseley, J.C. Mather, D. McCammon, J. Appl. Phys. 56, 1257 (1984).

7. D. McCammon, Nucl. Instr. and Meth. A 520 (2004).

8. Ch. Enns, Cryogenic Particle Detection Ch 1 1-34 (2005).

9. A. Goobar, S. Hannestad, E. Mortsell, H. Tu, J. Cosm. Astro. Phys. 6, 19 (2006).

10. E. Andreotti, C. Arnaboldi, P. de Bernardis, J. Beyer, C. Brofferio, M. Calvo, S. Capelli, et. al. Nucl. Instr. and Meth. A 572, 208, 11 (2007).

11. Ch. Kraus, B. Bornschein, L. Bonn, B. Flatt, A. Kovalik, B. Ostrick, E.W. Otten, J.P. Schall, Th. Thummler, Ch. Weinheimer Eur. Phys. J. C 40, 447 (2005).

12. The KATRIN collaboration, Nucl. Instr. and Meth. A 752, 14 (2005).

13. M. Galeazzi et.al., Phys. Rev. C, 63, 014302, (2000).

14. M. Galeazzi, N.S.F. Proposal for TES based MARE-1 (2006).

15. R.J. Gaitskell, Annu. Rev. Nucl. Part. Sci. 54, 315 (2004).

16. M. Tegmark, A. Aguirre, M.J. Rees, F. Wilczek Phys. Rev. D, 73(2):023505 (2006).

17. Collaborative Research: DUSEL R&D – Development of massive semiconducting detectors for a 1-tondark matter experiment, (grant proposal).

18. H.J. Maris J. Low Temp. Phys., 93, 355 (1993).

19. N. Mirabolfathi et al. Nucl. Instr. and Meth. A, 559, 417 (2006).

Chapter 3:

20. Ch. Enns, D. McCammon, J.Low Temp. Phys. 151, 1/2 (2008).

21. Ch. Enns, Cryogenic Particle Detection chapter 3 63-142.

22. J.C. Mather Appl. Opt. 21, 1125 (1982).

23. K. Irwin, Appl. Phys. Lett. 66, 1998 (1995).

24. K. Tsuji, J. Injuk, R. Van Grieken, X-ray spectrometry: recent technological advantage, ch 4.4 229-246.

25. S. Smith, S. Shapiro, J.L. Miles, J. Nicol Phys. Rev. Lett. 6. 686 (1961).

26. W.A. Simons, D.H. Dougless, Phys. Rev. Lett., 9, 153 (1962).

27. P.G. De Gennes, Rev. of Mod. Phys., Jan (1964).

28. J.C. Mather, Appl. Opt. 23, 584 (1984).

29. S.H. Moseley, J.C. Mather, D. McCammon, J.Appl. Phys. 56, 1257 (1984).

30. M. Galeazzi, D. McCammon, J. Appl. Phys. 93, 4856 (2003).

31. M. Galeazzi, Nucl. Instr. and Meth. A 520, 320 (2004).

Chapter 4:

32. K.S. Wood, D. Van Vechten, Nucl. Instr. And Meth. A, 314, 86 (1992).

33. R.A. Hein, J.W. Gibson, B.T. Matthias, T.H. Geballe, E. Corenzwit, Phys. Rev. Lett, 8, 10 (1962).

34. D. Pergolesi et al. Nucl. Instr. And Meth. A, 520, 311 (2004).

35. N. Gelfond, F. Tzikov, I. Igumenov, Thin Solid Films, 227, 2 (1993).

36. M.A. El Khakani, M. Chaker, B. Le Drogoff, Journ. Vac. Sc. Tech. 16, 2 (1998).

37. http://www.ajaint.com/systems orion.htm.

38. http://www.angstromsciences.com/technology/sputteringtechnology/index.html.

39. Cl. Chen, PhD. thesis University of Miami 2006.

40. M. Tinkham Introduction to Superconductivity ch. 4 (1996).

41. K.D. Irwin, G.C. Hilton, D.A. Wollman, J. M. Martinis, J. Appl. Phys. 83, 3978 (1998).

42. W.A. Little, Phys. Rev. 156, 398 (1967).

43. C.P. Poole et. al. Superconductivity.

44. M. Galeazzi, TES3 – talk "Flux flow noise in Transition Edge Sensors" http://www.phys.ufl.edu/tes3/program.html.

45. Y. Kunieda, D. Fukuda, M. Ohno, H. Takahashi, M. Nakazawa, T. Inou, M. Ataka, Jap. J. Appl. Phys. 2742 (2004).

46. R.J.Soulen, D.U. Gubser, J. Low Temp. Phys. 13, 498 (1973).

47. R.A. Hein et al., Phys. Rev. Lett. 8, 408, (1962).

48. L.B. Holdeman, et al. Journal de physique, C6, 608 (1978).

49. C.A. Linhares et al. Phys. Rev. B 73, 214525 (2006).

50. M. Strongin et al. Phys. Rev. B 1, 1078 (1970).

51. J. Kodama et al. J. Appl. Phys. 54, 4050 (1983).

52. Mc. Millan, Phys. Rev. 167, 2 (1968).

53. L.M. Abreu et al. Eur. Phys. J. B 37, 515 (2004).

54. A. Alessandrello, et al., Phys. Rev. Lett. 82, 513 (1999).

55. M. Galeazzi, D. Bogorin, C. Chen, Nucl. Instr. And Meth. A, 559, 453 (2006).

56. G. Petzow, Metallographic etching 2nd edition.

Chapter 5:

57. M. Galeazzi et al. J. Low. Temp. 151, (2008).

58. M. Galeazzi, D.F. Bogorin, F. Gatti, L. Parodi, ASC 08 submitted aug (2008).